IEEE Journal of
Microwaves

Received 1 May 2021; revised 1 August 2021; accepted 23 August 2021. Date of publication 28 September 2021; date of current version 7 October 2021.

Digital Object Identifier 10.1109/JMW.2021.3109277

Integrated Magnetics and Magnetoelectrics for Sensing, Power, RF, and Microwave Electronics

YIFAN HE, BIN LUO, AND NIAN-XIANG SUN (Fellow, IEEE)

(Invited Paper)

Department of Electrical and Computer Engineering, Northeastern University, Boston, MA 02115 USA

CORRESPONDING AUTHOR: Nian-Xiang Sun (e-mail: n.sun@northeastern.edu).

(Yifan He and Bin Luo contributed equally to this work.)

ABSTRACT As the rapid development of integrated magnetic and magnetoelectric, numerous novel devices including high performance on-chip transformers, inductors, filters, antennas, and sensors with unique advantages in power efficiency, size and tunability, etc. have been demonstrated. In this review, an overview of the development of magnetism and magnetoelectric will be firstly given. The conceptual illustration and materials used in integrated magnetoelectric will then be presented. Selections of on-chip devices from literatures will be shown to exemplify the integrated magnetic and magnetoelectric applications. Finally, the prospect and the direction of the future research will be discussed in the conclusion.

INDEX TERMS Magnetic, magnetoelectric, integrated devices, high frequency, sensing.

I. INTRODUCTION

Magnetic materials have a long history of usage since 4500 years ago when Chinese made the compass and also play an important role in modern technologies like motor, electrical generator, and transformer, etc [1]. With the development of solid state physics, the magnetic properties and theories beyond the static states have been discovered and utilized including the magnetostatic wave propagation, magnetization oscillation and spintronics, which enable a wide variety of new applications especially for high frequency integrated electronics and magnetic storage including waveguide [2], inductor [3], filter [4], phase shifter [5], Magnetoresistive random-access memory (MRAM) [6], spin-based transistor [7], oscillator [8] and sensor [9] etc.

Magnetoelectrics (ME) refers to the coupling between the magnetism and electricity and is one of the aspects of multiferroics which indicates the material presents two or more ferroic properties (ferroelectricity, ferroelasticity, ferromagnetism). It has been shown that the two-phase ME heterostructure that couples through the mechanical strain can generate much larger ME coupling compared with its single phase counterpart [10]. The ME coupling effect provides a new methodology to mediate and monitor the magnetism in the magnetic material, and hence brings numbers of new potential features to the devices mentioned above. The ME coupling can be divided into two categories, namely direct ME effect (DME) where the electric polarization is controlled by the magnetic field and converse ME effect (CME) where the magnetization is controlled by the electric field.

Since the emerging and prosperity of complementary metal-oxide-semiconductor (CMOS) and thin-film technology, both magnetic and magnetoelectric materials have been integrated into the batch fabrication and incorporated in numbers of compact, power efficient on-chip devices. Among them, the integrated magnetic material serves versatile functions and will be elaborated later, DME is majorly used for sensing applications [11] and energy harvesting [12] where the external magnetic field is coupled to magnetic phase and generate an electric filed at output, whereas the CME is utilized to achieve numbers of integrated electric field tunable devices including tunable inductor [13], filter [14], etc. The newly demonstrated nanoelectromechanical system (NEMS) transmitting ME antennas [15] also rely on the CME. A selection of on-chip radio frequency (RF) /microwave, power and sensing devices will be shown in this paper to elaborate the typical application structures, features and benefits brought by the integrated magnetics and magnetoelectrics.

This work is licensed under a Creative Commons Attribution 4.0 License. For more information, see https://creativecommons.org/licenses/by/4.0/

II. MAGNETOELECTRIC EFFECT, MATERIALS AND RELEVANT PHYSICAL MECHANISMS

As one category in multiferroic material, ME material shows ferroelectricity and ferromagnetism simultaneously and hence provides a potential methodology for achieving multiple functions in one device and subsequently device miniaturization [10]. The first experimental demonstration of ME effect was achieved in single phase Cr_2O_3 material by Dzyaloshinski in 1960 [16], numerous efforts have been put into discovering new material for larger ME coupling effect. However, researchers found in 2000 that in respect to the transition metal atomic orbital, the conditions forming the ferroelectricity and ferromagnetism excludes each other, which explains the difficulty of synthesize highly efficient material with large ME effect under various temperatures [17]. On the other hand, strain mediated two-phase ME composite, which typically consists of an electrostricive/piezoelectric phase and a magnetostrictive phase, is capable to overcome the physical limitation of its single-phase counterpart and present stronger ME coupling. The two-phase ME composite utilizes the material strain to convert the magnetic field to electric polarization in DME case and to convert electric field to magnetization in CME case. To quantify the strength of ME coupling, the direct and converse ME coefficient are named and defined as [18]:

$$\alpha_{Direct} = \frac{\partial P}{\partial H} \tag{1}$$

$$\alpha_{Converse} = \frac{\partial M}{\partial E} \tag{2}$$

In the above equations, P is the electric polarization, H is the applied magnetic field, M is the magnetization and E is the applied electric field.

To better describe the ME coupling condition in designing practical applications or analyzing the experimental results, magnetically induced voltage ME coefficient is defined and widely used [19]:

$$\alpha_{ME} = \frac{\partial E}{\partial H} \tag{3}$$

where H is the applied magnetic field and E is the induced electric field.

It is clear that for two-phase ME composite material, the intrinsic material properties and the interface condition are of significance to ensure a decent coupling condition. As an example, the theoretical upper limit of ME coefficient of a L-L (longitudinally magnetized longitudinally poled) configuration ME composite can be given as [20]:

$$\alpha_{ME} = \frac{n d_{33,m} d_{33,p}}{n s_{33}^{E}\left(1 - {k_{33}}^{2}\right) + (1-n)\, s_{33}^{H}} \tag{4}$$

where $d_{33,m}$ and $d_{33,\mathrm{p}}$ are the longitudinal piezomagnetic and piezoelectric coefficient, k_{33} is the electromechanical coupling coefficient of the piezoelectric layer, s_{33}^{E} and s_{33}^{H} are the elastic compliance for the piezoelectric and magnetostrictive layers, and n is a thickness fraction of the magnetostrictive layers.

The strong ME coupling effect can boost the performance of DME based sensing and energy harvesting in terms of the sensitivity or energy conversion efficiency, as well as the function tunning range of CME based devices. In the rest part of the section, we will present various material choices in both piezoelectric/electrostrictive phase and magnetostrictive phase that are widely adopted for achieving strong ME coupling. For the CME-based devices, since device features are typically enabled by different magnetic film properties and CME is adopted to alter these properties for reconfigurability, we will discuss the magnetic properties tuning mechanisms induced by the strain brought by CME in this section and elaborate the material choices and configurations in the following sections that focus on the devices.

A. CME INDUCED MAGNETIC PROPETY TUNING MECHANISMS

As previously mentioned, unlike DME whose applications typically requires a strong ME coupling, CME-based applications focus more on the reconfigurability brought by the strain-mediated magnetic properties. For a simple multiferroic composite with a magnetic thin film deposited or glued on a piezoelectric layer, a strain generated in piezoelectric layer by applied electric field is transferred to magnetic thin film. Due to the induced magnetoelastic energy and the tendency of energy minimization, the influence of the strain upon the static and dynamic behavior of magnetization can be quantitively denoted by the voltage induced effective in-plane magnetic field [21, 22], which is given as:

$$\Delta H_{eff} = \frac{3\lambda_s \cdot Y \cdot d_{eff} \cdot E}{\mu_0 M_s} \tag{5}$$

where λ_s is the saturation magnetostriction of the magnetic film, Y is the Young's modulus of the magnetic film, M_s is the saturation magnetization of the magnetic film; d_{eff} is the effective piezoelectric coefficient of the piezoelectric layer, and E is the electric field applied on the piezoelectric layer.

In this part, we will discuss two magnetic property tuning mechanisms that are induced by the strain, including E-field tuning ferromagnetic resonance (FMR) and E-field tuning permeability. The abovementioned mechanisms serve as the basis for the reconfigurability of multiple integrated high frequency, power and sensing devices. There are some more tuning mechanisms including E-field tuning magnetoresistance and E-field tuning M-switching, the former one is utilized to adjust the sensitivity and detection range of magnetoresistance sensors [23], the later one is majorly adopted for magnetic storage devices like ME random access memory (MERAM) to control the magnetization rotation [24]. These two mechanisms will not be elaborated in this work considering their rather minor applications.

1) E-FIELD TUNING FERROMAGNETIC RESONANCE

FMR refers to the resonance happens when the spontaneous Larmor precession frequency of magnetization coincides with the external electromagnetic wave excitation. In this case, the external excitation signal is absorbed for magnetization precession and attenuated due to the presence of the magnetic damping. FMR was first experimentally demonstrated by Griffiths in 1946 [25]. In 1951, Kittel proposed Kittel equation [26] that determined the FMR frequency:

$$f_{FMR} = \gamma\sqrt{(H_{dc}+H_a+(N_y-N_z)4\pi M_s)(H_{dc}+H_a+(N_x-N_z)4\pi M_s)} \quad (6)$$

In equation 6, γ is the gyromagnetic ratio; H_{dc} is the applied DC magnetic field; H_a is the spontaneous magnetic anisotropy field, N_x, N_y, and N_z are the demagnetizing factors determined by the dimension of the magnetic material.

It Is Clearly Shown in Equation 6 With the Effective Magnetic Field Induced By the strain, H_{dc} Changes and Hence Shift the FMR frequency.

For the magnetic film exhibiting in-plane magnetization parallel to E-field induced effective magnetic field, the tunability of the FMR frequency can be approximated as [27]:

$$\frac{\Delta f}{f} \approx \frac{1}{2}\frac{\Delta H_{eff}}{H_a} \quad (7)$$

For the magnetic film exhibiting out-of-plane magnetization parallel to E-field induced effective magnetic field, the tunability of the FMR frequency can be approximated as:

$$\frac{\Delta f}{f} \approx \frac{\Delta H_{eff}}{H_a - M_s} \quad (8)$$

Fig. 1(a) presents a typical test setup for FMR absorption of magnetic material thin films. The FeGaB/PZN-PT ME composite was placed on top of a transmission line. The electromagnetic wave propagated in the transmission line was coupled with the magnetic material and a notch in the transmission coefficient S_{21} spectrum would appear at the corresponding FMR frequency due to the energy absorption. The S_{21} spectrum of the FeGaB/PZN-PT ME composite in the self-biased condition (without the excitation of bias magnetic field) is shown in Fig. 1(b) [21]. It can be noted that the FMR where the maximum absorption peak resides can be tuned by electric fields in the self-bias condition over a wide range of frequency from 1.75 GHz at zero electric field to 7.57 GHz at 6 or 8 kV/cm, with a tunable frequency range of 5.82 GHz. The wide electrostatically tunable frequency range corresponding a mean tunable frequency per unit electric field of 15 GHz·cm·kV^{-1} and a tuning ratio of f_{max}/f_{min}=4.3 have been achieved.

2) E-FIELD TUNING PERMEABILITY

Permeability is another crucial parameter of magnetic materials. High permeability materials are widely used in transformer and inductor applications to concentrate the magnetic flux and hence increase the inductance and magnetic coupling factor. With the need of the reconfigurability, the ME composite can serve as the magnetic core for these devices.

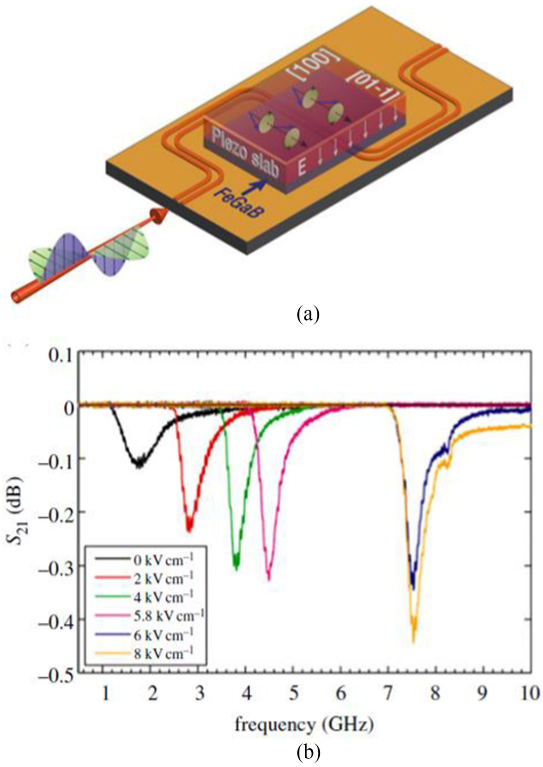

(a)

(b)

FIGURE 1. (a) Microwave absorption test setup for FeGaB/PZN-PT ME composite. (b) Electric field dependence of the transmission coefficient (S_{21}) spectra of FeGaB/PZN-PT ME composite. (Reproduced from [21]).

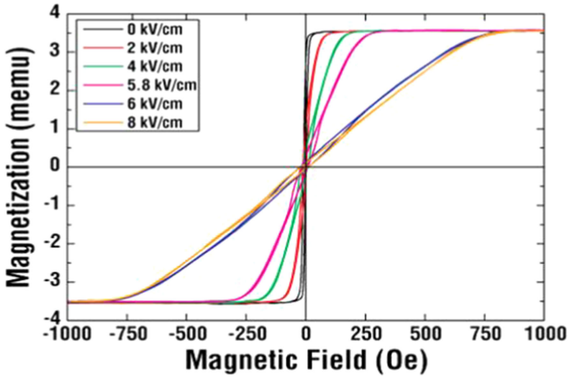

FIGURE 2. Magnetic hysteresis loops of the FeGaB/PZN-PT multiferroic heterostructure under different external electric fields. (Reproduced from [21]).

The effective field generated by the strain in ME composite changes the magnetic anisotropy field and thereafter the easy axis direction of the magnetic material. Therefore, the effective permeability describing the magnetization response under the applied magnetic field in a certain direction change with the applied electric field applied on the ME composite.

To exemplify the tunning mechanism, the magnetic hysteresis of FeGaB/PZN-PT ME composite under different electric fields is shown in Fig. 2 [21]. The tunable hysteresis loop shows an in-plane anisotropy field ranging from 20 Oe at 0 kV/cm and 700 Oe at 6 kV/cm. The different slopes of

TABLE 1. Comparison of Commonly Used Ferro/Piezoelectric/Electrostrictive Materials for ME Applications

	Soft PZT	Hard PZT	PMN-PT	PZN-PT	AlN	AlScN	BiFeO3-based ceramics
d_{31} (pC/N)	-175~-274	-58~-140	-1800		-2		
d_{32} (pC/N)			900	-3800			
d_{33} (pC/N)	400~593	149~320	2000	2800	3.5~4	24.6~27.6	42
T_c (˚C)	195~360	300~330	145	160	>2000	>600	810~830
ε_r	1850~2870	325~1375	~6000	~6000	~10	9~24	<200
$\tan\delta$	1.25~2.5	0.2~0.4	0.0042	0.0047	0.0005	0.004~0.006	0.005~0.55
References	[29]	[29]	[35],[37]	[34],[37]	[31-33]	[159-164]	[165-168]

the hysteresis loop indicate the applied electric field have changed the magnetization response and hence the effective permeability in in-plane direction.

To quantify the effective permeability μ_{eff} with the presence of strain, the following equation is given in [13]:

$$\mu_{eff} = \frac{4\pi M_s}{H_{eff}} + 1 \tag{9}$$

where the effective magnetic anisotropy field can be given as:

$$H_{eff} = H_a + \Delta H_{eff} \tag{10}$$

where H_a is defined in equation 6 and ΔH_{eff} is defined in (5) as the electric field induced effective anisotropy magnetic field in the magnetic films.

B. PIEZOELECTRIC/ELECTROSTRICTIVE MATERIALS FOR MAGNETOELECTRICS

Among piezoelectric/electrostrictive materials, lead zirconate titanate (PZT), lead magnesium niobate–lead titanate (PMN-PT), lead zinc niobate–lead titanate (PZN-PT) and aluminum nitride (AlN) have been widely used in integrated ME devices to convert electric excitation to strain. Table 1 shows a cross comparison of the most commonly used piezoelectric/electrostrictive materials for integrated ME applications. PZT is a polycrystalline ceramic ferroelectric material with a high electromechanical coupling coefficient and an effective piezoelectric coefficient of −200 to −300 pC/N [28] at morphotropic phase boundary (MPB) composition corresponding to Zr/Ti ratios of about 58/42. The PZT piezoelectric ceramic also has the advantages of low-cost and easier shaping process [29]. The main drawback of PZT materials is that the contamination during the process is often unavoidable due to the lead in it, which greatly degrades its application in magnetoelectric devices [30]. Moreover, the relatively high acoustic loss of the PZT film at high frequency range prevents it from achieving an efficient ME coupling. In Table 1, PZT materials are classified into hard and soft PZTs, where the hard PZT materials usually have smaller piezoelectric coefficient with higher energy efficiency. Depending on the circumstance of the specific applications, various types of PZT materials are commercially available. Different from the PZT film, aluminum nitride (AlN) is a textured polycrystalline non-ferroelectric material with an advantage of lower loss tangent and compatibility with CMOS technology. Another unique advantage of AlN is its high electric Curie temperature, which is desirable for electronics applications working under high temperature of inferior heat dissipation environment. However, the moderate piezoelectric coefficient of about −2 pC/N makes it unsuitable for ME devices requiring high ME coupling [31]–[33].

Compared with PZT and AlN, lead magnesium niobate–lead titanate (PMN-PT) and lead zinc niobate–lead titanate (PZN-PT), as single crystal ferroelectric materials, show larger piezoelectric coefficients and lower loss tangents. The piezoelectric performance of these materials highly depends on their composition and crystal orientation. The composition here means the element ratio of rhombohedral phase (PZN or PMN) and tetragonal phase (PT). The PZN-PT composition that induce MPB with (001) crystal cut can give a d_{33} piezoelectric coefficient as high as 2800 pC/N [34]. For the PMN-PT film, a 31% PT and optimized cut give a d_{31} of about -1800 pC/N and a d_{33} of about 2000 pC/N [35]. Although the forementioned two materials deliver superior piezoelectric performance, the difficulties of composition control during the deposition of these materials may induce the lack of performance repeatability. The grain growth of these single crystal materials is also challenging. Two major deposition methods include flux method and Bridgman method [36].

C. PIEZOMAGNETIC/MAGNETOSTRCTIVE MATERIALS FOR MAGNETOELECTRICS

In general, the desired properties of piezomagnetic/magnetostrictive phase in ME composite for achieving a strong ME coupling are high saturation magnetostriction λ_s and high piezomagnetic coefficient $d\lambda/dH$. Depending on the specific applications, other magnetic and elastic properties of the materials may also be considered. The low magnetic loss tangent, low FMR bandwidth and low coercive field are essential for high frequency application. Some particular properties like ΔE effect where the Young's modules of materials vary with the applied magnetic field, are also needed for specific applications including sensors.

A cross-comparison of commonly used piezomagnetic/magnetostrictive materials for ME composite is given in Table 2 including Terfenol-D ($Tb_{0.7}Dy_{0.3}Fe_2$), Galfenol ($Fe_{81}Ga_{19}$), FeGa, FeCoSiB, FeGaB, FeBSiC (Metglas) and FeGaC.

Based on the Terfenol-D with the largest magnetostriction, the Terfenol-D/PZN-PT composite with giant electric field induces effective magnetic anisotropy field of 3500 Oe, corresponding to a magnetoelectric coefficient of 580 Oe·cm/kV [44]. The magnetoelectric coefficient is almost 4 times

TABLE 2. **Comparison of Commonly Used Piezomagnetic/Magnetostrictive Materials for ME Applications**

	Terfenol-D	Metglas	FeGa	FeGaB	FeCoSiB	FeGaC
λ_s (ppm)	1600	30	400	70	158	81.2
$(d\lambda/dH)_{max}(\times 10^{-6}/Oe)$	2.4	3.8	1.5	7		9.71
μ_r	10	45000	73 at 50 kHz	~400	~145 at 600 MHz	
T_c (˚C)	650	395	675			674
References	[21],[38],[50]	[21],[43]	[21],[39],[40] [51], [52]	[21],[42],[53]	[41],[54]	[169-170]

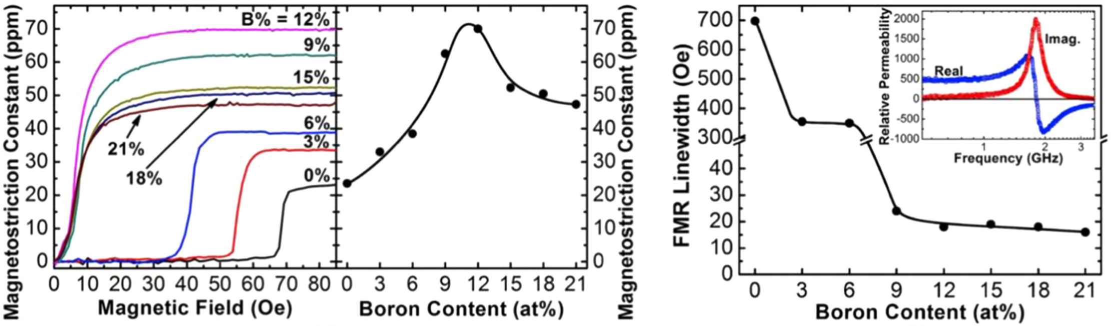

(a) (b)

FIGURE 3. **(a) Boron content dependent magnetostriction property of FeGaB thin film material. (b) Boron content dependent FMR linewidth of FeGaB thin film material. (Reproduced from [48]).**

of that in Fe_3O_4/PZN-PT [22]. Even though Terfenol-D exhibits giant saturation magnetostriction of 1600 ppm, it is lossy and has a high saturation field of several kOe, which induces a relatively small piezomagnetic coefficient. Compared with Terfenol-D, binary FeGa alloys show a high saturation magnetostriction constant of 400 ppm for single crystals (Galfenol($Fe_{81}Ga_{19}$)) and 275 ppm for directional solidified polycrystalline alloys (FeGa), a low saturation field of about 100 Oe and a high saturation magnetization of 18 kG. However, the FeGa films have a large FMR linewidth of 450-600 Oe at X band and strong loss at microwave frequencies [45]. The shortcoming indicates that the FeGa alloys are far from being an ideal magnetic material to be incorporated into RF/microwave magnetoelectric devices. Boron (B), as a well-known metalloid element, has been added into the FeGa and FeCo films to improve their magnetic properties. It has been experimentally demonstrated that the addition of B in FeCo films contributes to an excellent soft magnetization and microwave properties by refining the grain size and diminishing magnetocrystalline anisotropy [46,47]. Moreover, the addition of Boron in the composition of FeCoSiB and FeGaB thin films contributes to the demonstration of giant ME coefficients and low loss tangents in ME devices RF/microwave devices.

FeGaB material exhibits excellent performance on magnetic softness, saturation magnetization, saturation magnetostriction, piezomagnetic coefficient, ΔE effect, magnetomechanical coupling factor and has been regarded as the most ideal piezomagnetic film material for ME devices [48]. As indicated in [48], with the addition of B rising from 0% to 21% in FeGa, the coercivity H_c decreased from about 100 Oe to 1 Oe and the effective anisotropy field H_k dropped from 120 Oe to 15 Oe due to the material phase transition (MPB). The reduced coercivity and anisotropy significantly enhances magnetic softness. Additionally, as shown in Fig. 3(a), the B content induced phase transition results in a lower threshold magnetic field to generate a magnetostrictive response. The maximum magnetostriction of 70 ppm achieved at 12% B content was three times of that of the binary FeGa films. The FMR linewidth of FeGaB films also dropped dramatically from 700 Oe for binary FeGa films to 16 Oe at 21% B content. The maximum piezomagnetic coefficient of the FeGaB films has been reported as about 7 ppm Oe^{-1}, which is much higher than multiple magnetostrictive materials,including Terfenol-D (Tb-Dy-Fe), Galfenol (Fe-Ga) and Metglas (FeBSiC). The comparison was made in [21] and graphically shown in Fig. 4. The maximum piezomagnetic coefficient can be further enhanced to 12 ppm Oe^{-1} after annealing due to the effective release of residual stress inside the film and the reduction of total anisotropy energy [49].

III. INTEGRATED MAGNETIC AND MAGNETOELECTRIC FOR POWER, RF, AND MICROWAVE APPLICATIONS

Integrated magnetic materials play a significant role in enabling high performance or unique features in multiple power, RF and microwave devices. The static and dynamic properties of these materials are widely utilized to achieve high efficiency magnetic flux guide, frequency selectivity

TABLE 3. Integrated Magnetic and Magnetoelectric Devices for Power, RF, and Microwave Applications

Physical Properties or Mechanisms	Devices	References	Key Device Specifications
High permeability	Integrated inductor	[3],[58],[61],[63],[65-68]	L=3 nH @ up to 3 GHz Q>10 @ 0.5 GHz [3]
	Integrated transformer	[55],[56],[57],[59],[62]	L=565 nH @ up to 50 MHz Coupling factor=0.97 [62]
CME: E-field tuning permeability	Integrated E-field tunable inductor	[13]	L=1.2-3.5 nH @ up to 2 GHz Q=~2-5.2 @ 0.5 GHz [13]
FMR/magnetostatic wave transmission CME: E-field tuning FMR and magnetostatic wave transmission	Integrated filter/integrated E-field tunable filter	[4],[14],[82],[83]	f_{centre}=3.78 GHz Insertion loss=1.73 dB H field tunability: 5 MHz/1 Oe E field tunability: 55 MHz/1 (kV/cm) [14]
Mechanical resonance and ΔE effect	Integrated E-field tunable bandpass filter	[86]	f_{centre}=93.165 MHz Insertion loss=3.4 dB H field tunability: 5 kHz/1 Oe E field tunability: 2.3 kHz/1 V [86]
DME/CME	Integrated ME antenna	[15],[107],[108]	NPR: f_r= 60.68 MHz, Q=1110 FBAR: f_r=2.53 GHz, Q=632 Antenna gain= -18 dBi [15]

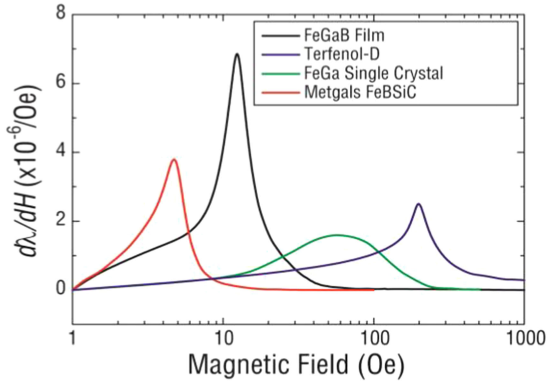

FIGURE 4. Piezomagnetic coefficients ($d\lambda/dH$) of different types of magnetostrictive alloys. (Reproduced from [21]).

by spontaneous resonance, magnetostatic wave guide, spin controlling, etc. As previously mentioned, by introducing strain-mediated magnetoelectric composites, the magnetic properties of these material can be altered by applying electric field, which provides possibilities for novel electrostatically highly energy-efficient, compact, miniature and lightweight tunable devices for power, RF and microwave electronics. In this section, several integrated magnetic and magnetoelectric devices including high performance transformer, inductor with laminated magnetic core, voltage tunable inductor, E- and H- field tunable bandpass filter and NEMS ME antennas are presented. The selected applications are good representatives for power components, basic circuit components, RF and microwave signal processing block and RF and microwave signal transmitting/ receiving block, respectively. A summary of the applications presented in this section is given in Table 3.

A. ON-CHIIP TRANSFORMER, INDUCTOR WITH INTEGRATED MAGNETIC CORE AND VOLTAGE TUNABLE INDUCTOR WITH ME COMPOSITE

The inductor and transformer are two types of devices whose operations rely on the magnetic flux variation and energy conversion. As the rapid development of integrated RF, microwave and power circuits, the high Q, compact inductor with sufficiently large inductance and transformers with high power efficiency and coupling coefficient are highly demanded. The integrated magnetic materials, serve as the magnetic core, can boost the inductance and the transformer coupling condition by concentrating the magnetic flux generated during the operation. The mostly used magnetic materials for core are always high-permeability materials including permalloy (NiFe) [55], NiFeW [56], NiFeZn [57], NiZn ferrite [58],

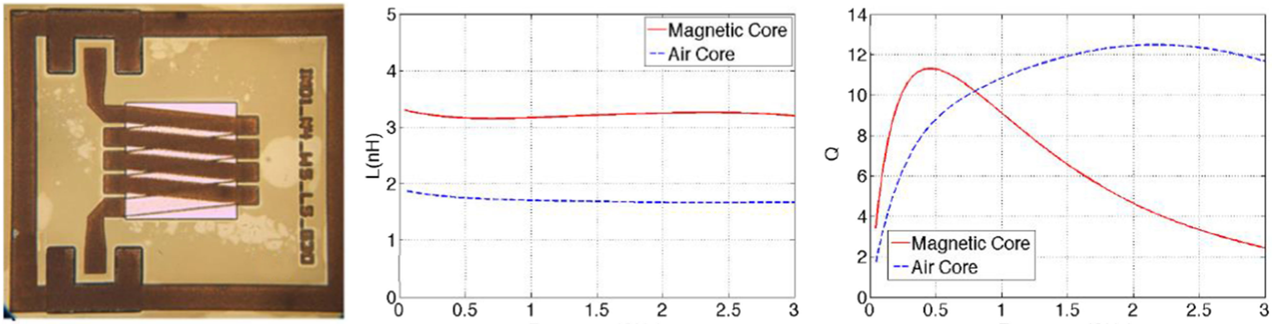

(a)

(b)

(c)

FIGURE 5. (a) Optical image of the on-chip inductor with solenoid structure. (b) Inductance measurement result of inductors with magnetic core and air core. (c) Quality factor measurement results of inductors with magnetic core and air core. (Reproduced from [3]).

FeCoSiB [59], FeCoCu [60], FeGaB [3], [61], etc. However, there are two limitations brought by the integrated magnetic core: 1). The relatively thick magnetic core in on-chip devices induces large eddy current loss during high frequency operation, which limits the quality factor; 2). The FMR of the magnetic core causes energy absorption in the corresponding frequency range, which diminishes the power efficiency and working frequency range. To mitigate the high eddy current loss issue, the integrated magnetic core was engineered as a laminated structure [61]–[63] with thinner magnetic material layers and isolation spacer in between. The thinner magnetic material has higher equivalent resistance and hence reduce the eddy current induced by the time-varying magnetic field. As for the loss caused by FMR, the Kittel [64] equation suggests that by determining proper magnetic film dimensions, the demagnetizing factor can be manipulated such that the FMR frequency is higher, which subsequently expand the operational frequency range [63]. The most commonly adopted inductor and transformer coil structures include solenoid and spiral/planner structure, where the solenoid structure [55], [58], [61], [63] incorporates the magnetic core between the wires at upper and lower layers whereas in the spiral/ planer [65]–[68] structure the magnetic core layer is deposited beneath or between the planer wires to form the magnetic circuit.

In 2014, Gao [3] reported a series of integrated inductors using multilayer FeGaB (100 nm)/Al_2O_3 (5 nm)/FeGaB (100 nm) sandwich structure as the magnetic core. The authors adopted solenoid structure for the inductor design and the optical image of the as-fabricated device is shown in Fig. 5(a). As shown in Fig. 5(b), compared with the air core inductor with same dimensions, the magnetic core boosted the inductance by nearly 100% in the frequency range of up to 3 GHz. The inductance showed a flat characteristic with a peak inductance of over 3 nH, which indicated that the laminated magnetic core was of help to eliminate the eddy current loss in high frequency range and the energy loss contributed by FMR. The quality factor in the frequency range of up to 3 GHz is shown in Fig. 5(c), where the peak quality factor of the inductor with magnetic core was over 10 and showed a better performance compared to the air core inductor in the relatively low frequency.

Mullenix [62] reported an on-chip micro-transformer with integrated laminating magnetic core in 2013. The device turns ratio is 1:1. As shown in the Fig. 6(a), the transformer has a dual-coils solenoid structure. The authors fabricated a series of devices with 8 turns coils, 16 turns coils, 32 turns coils, and 32 turns coils with air core for comparison. The cross-sectional view of the coil is shown in Fig. 6(b), a 2.8 μm thick NiFe/AlN laminated film was adopted as magnetic core and the optimized thickness of the insulating AlN layer was determined to be 7 nm. The inductances of a pair of inductors with a 500 μm× 5.6 μm core connected in series with difference turn numbers are shown in Fig. 6(c). The 32 turns AC in the plot indicates the measurement result of air core inductor. The introducing of the magnetic core boosted the inductance by 60 times, namely 565 nH in the operating frequency range. Fig. 6(d) shows the maximum Q factor achieved by 32 turns magnetic core transformer was 6.3 and the maximum coupling factor is 0.97, indicating a superior coupling between the primary and secondary coil. The results show the advantage of adopting laminating magnetic core since the pure magnetic material core with same thickness has lower roll-off frequency than the designed operation range.

Tunable RF inductors provide another possible solution for tackling the trade-off between inductance, quality factor and operating frequency range, since the external electric signal can lead to the control and improvement of these 3 parameters at the same time. There have been two main branches of control strategies for tunable inductors in microelectromechanical systems (MEMS). One mechanism is to adjust the turns or numbers of inductor coils. Based on this, Park changed the turns or length of inductor coils by MEMS switch and achieved an operation frequency of 2.4 GHz, a Q-factor of 3 and extremely large tunability of 187.5% [69]. The main drawback of this MEMS switch control strategy is the discrete tunability of inductance limited by the number of switches [69, 70]. In order to overcome this shortcoming, the inductor coupling control method with a secondary coil was put forward and applied to the fabrication of related devices, with

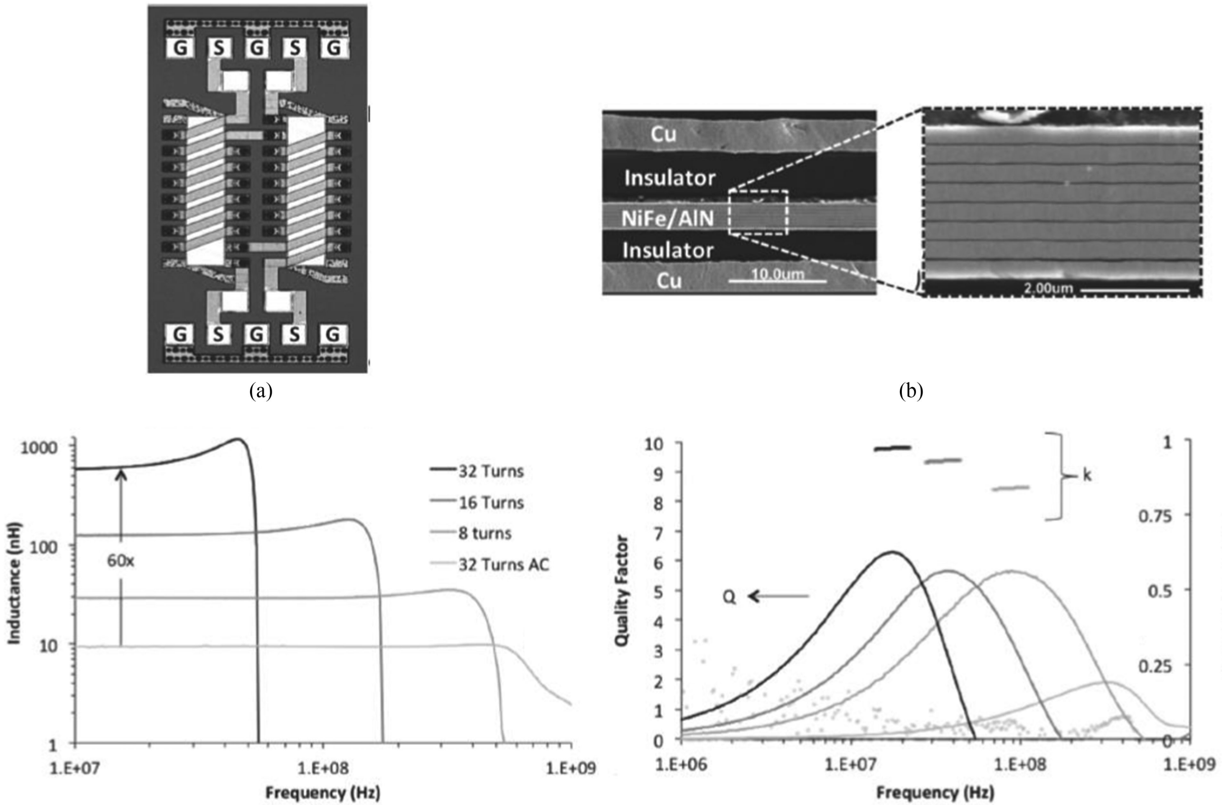

(a) (b)

(c) (d)

FIGURE 6. **(a) Optical image of the on-chip transformer. (b) Cross-sectional view of the coil. Measured (c) inductance, (d) quality factor and coupling coefficient for the devices with 500 μm X 5.6 μm core with 8, 16, and 32 turns. The "32 Turns AC" refers to the air core transformer of identical geometry with 32 turns. (Reproduced from [62]).**

an operating frequency ranging from 4.35 GHz to 7 GHz, a quality factor of ∼10 and an inductance tunability from ∼30% to ∼90% [71], [72]. However, the related work was greatly limited by the complicated structure and fabrication procedure. Another perspective is to change the properties of the magnetic core or the magnetic field distribution in it. Following this direction, researchers tried to control the magnetic flux by thermal actuation [73] or metal shield [74]. DC current was also widely used to modify the properties of magnetic core. For example, Salvia realizes a 40% increase in inductance, an inductance tunability of 15% and a Q-factor from 5 to 11 in the tunable on-chip inductors operating up to a frequency of 5 GHz using patterned permalloy laminations [67]. Unfortunately, both methods exhibit limited inductance tunability, high power consumption, significant thermal effect and excessive noise [67], [75]–[77].

With the development of magnetoelectric materials, researchers tended to use ME coupling to adjust the permeability of magnetic core and tune the inductance, aimed at improving the energy efficiency, reducing joule heating and increasing inductance tunability. The CME tuning mechanism is elaborated in Section II. In order to ensure higher inductance density and efficient utilization of magnetic film, the most popular spiral and solenoid structures have been widely used in electrostatically tunable inductor. A solenoid type magnetoelectric inductor fabricated with a layered multiferroic composite core was proposed by Lou, which consisted of two layers of Metglas magnetic ribbons and one PZT piezoelectric slab [78]. The inductance showed a strong electric field tunability, with maximum inductance change of 450%, 250%, and 50% for operation frequencies of 1 kHz, 100 kHz, and 5 MHz, respectively. The estimated energy consumption to achieve maximum tuning 450% is only about 1.3 mJ, indicating that the fabricated tunable magnetoelectric inductors were essentially passive and energy efficient and achieved a giant tunability. Due to the decreased permeability, increased skin depth and reduced core eddy current loss, the quality factor is improved from about 3 at zero electric field to about 8.5 at an external field of 12 kV/cm. The giant tunability achieved in such magnetoelectric inductors with low power consumption makes them ideal candidates for novel power efficient and compact electronic devices. In order to extend the operation frequency range and enhance the quality factor by reducing the eddy current loss, Lin fabricated PZT/Metglas/PZT voltage tunable inductors with single layer Metglas film and multiple piezoelectric slabs [79]. An 80% increase in Q-factor, 10 times of extension in operational frequency and 3 times of enhanced quality factor were observed. In addition, a 150%

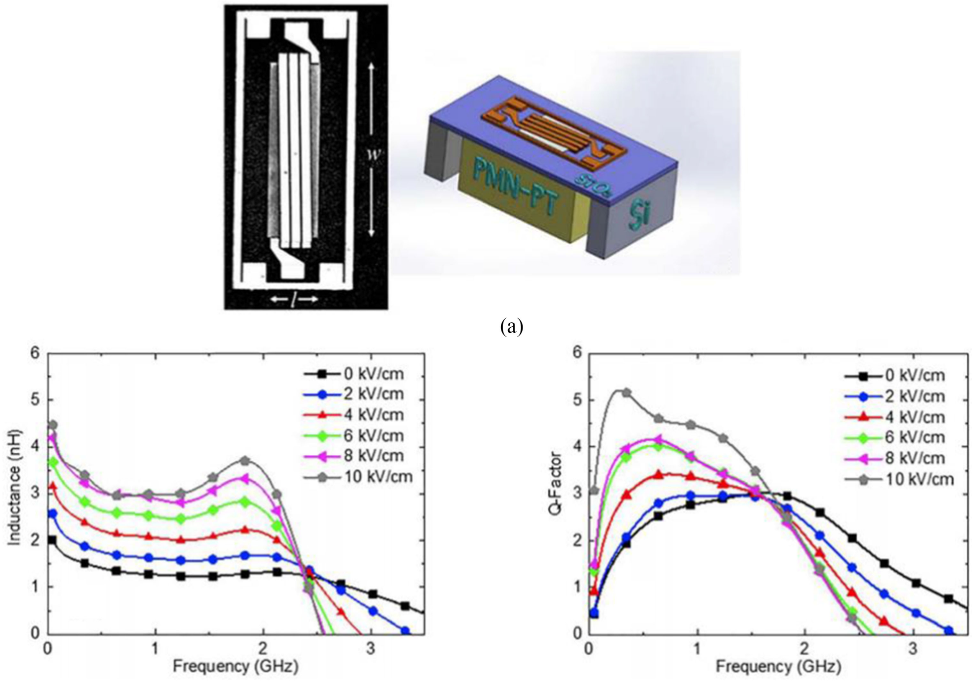

(a)

(b)

(c)

FIGURE 7. Integrated gigahertz FeGaB/Al_2O_3/PMN-PT voltage tunable ME inductor. (a) Optical image and structure model of integrated voltage tunable inductor with 3.5 turn and a magnetic film of 340 μm X 800 μm. (b) Measured inductance and (c) Q-factor of integrated FeGaB/PMN-PT tunable inductor with applied electric field from 0 to 10 kV/cm. (Reproduced from [13]).

improvement in quality factor and 100 times of extension in operational frequency could be found in ME inductors with a single PZT slab, whereas a 235% improvement in quality factor and 200 times of extension in operational frequency were realized in its double PZT slabs counterpart.

Though the PZT/Metglas/PZT ME inductors show a high performance in quality factor, inductance density and a giant tunability of 450% in the kilohertz frequency band, the Metglas/PZT multiferroic heterostructures are not applicable for the gigahertz applications due to their low FMR frequency. In addition, these inductors fail to realize compatible integration on CMOS circuits, which prevents their applications in RF/microwave electronics. To realize gigahertz range frequency operation, Chen has recently demonstrated a voltage tunable GHz integrated magnetic inductor by using the FeGaB/Al_2O_3/PMN-PT magnetoelectric composites, as shown in Fig. 7(a) [13]. Compared with materials like NiZn, the high permeability further improved by annealing, FMR frequency of 1.85 GHz with a narrow FMR bandwidth of 16∼20 Oe, large magnetostriction of FeGaB films lead to high inductance density, operation band in GHz range, relatively low magnetic loss and high frequency tunability, respectively. The inductor showed a relatively constant inductance and quality factor value in the frequency range of 0.5 to 2 GHz. The alumina spacer reduced the thickness of single-layer magnetic material, thereby increasing the sheet resistance and reducing the eddy current loss. The E-field tunability test results shown in fig. 7 (b) and (c) indicate that in this frequency range, with an applied electric field up to 10 kV/cm, the inductance rises from 1.2 to 3.5 nH and the quality factor rises from 2.7 to 5.2. The device achieved a maximum inductance continuous tunability of 191% at 1.5 GHz, which was significantly larger than other integrated inductors tuned by magnetic flux, DC bias current and coil coupling.

B. INTEGRATED RF AND MICROWAVE FILTERS AND VOLTAGE TUNABLE FILTERS WITH ME COMPOSITES

Filter is an essential component in RF/microwave signal processing circuits and blocks. There are several types of filters where the integrated magnetic and magnetoelectric materials function as a core part. In a typical filter based on lumped element [80,81], the magnetic materials serve as the core of inductors in the filter topology and the function is similar as forementioned inductor components. FMR absorption and magnetostatic wave manipulation properties of magnetic materials are also widely utilized for achieving band-stop and band-pass characteristics. Band-stop filters utilizing FMR absorption typically consist of a transmission line that couples with the magnetic materials. When the frequency of electromagnetic wave propagating in the transmission line coincides with FMR frequency of the material, a maximum attenuation and hence a stop band is generated. Multiple materials including transition metal [82], ferrite [83]–[85] and soft magnetic composite [4] are adopted for these band-stop filters. Magnetostatic wave manipulation property in ferrite is utilized to achieve non-reciprocal band-pass characteristic [14], which

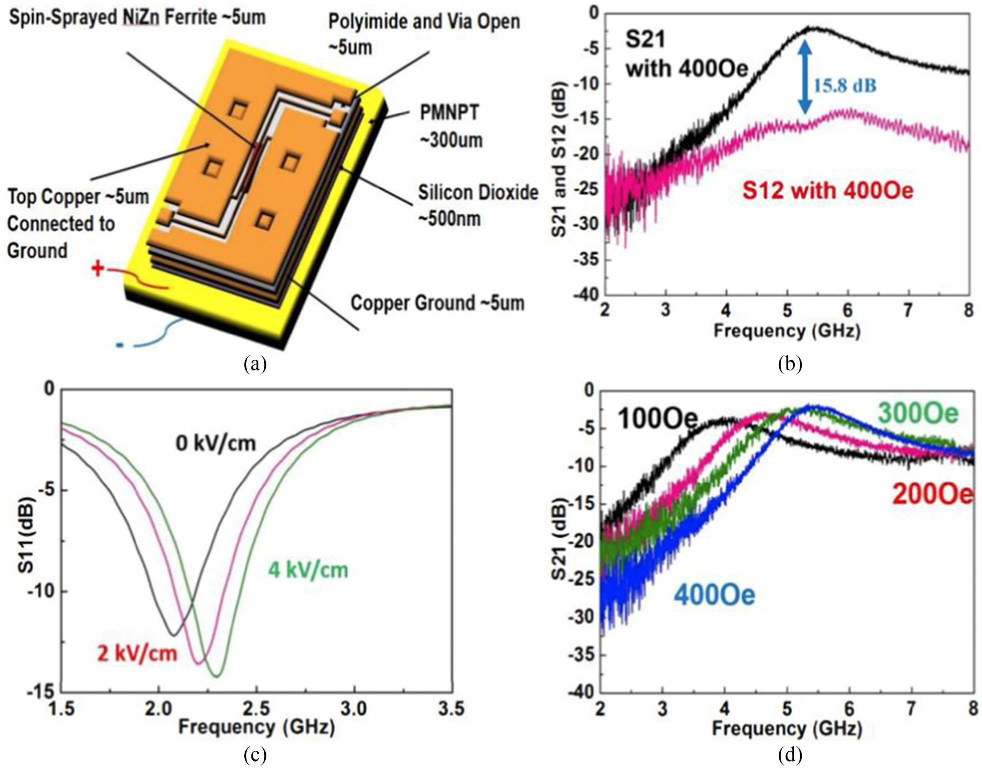

(a) (b)

(c) (d)

FIGURE 8. **Integrated NiZn/PMN-PT dual E- and H-field tunable ME band-pass filter. (a) Schematics of integrated tunable inductor. (b) S$_{12}$ and S$_{21}$ under a bias magnetic field of 400 Oe. (c) S$_{11}$ under different bias electric fields. (d) S$_{21}$ under different bias magnetic fields. (Reproduced from [14]).**

will be elaborated later in this part. The third type of integrated filter utilizes the mechanical resonance to realize frequency selectivity [86], where the input excitation signal is transformed into acoustic wave at the input resonator and propagate to the output resonator thorough the released material layer.

Reconfigurability is a crucial feature in filter design considering the need for wide band operation, the size of the signal processing block and the yielding cost. MEMS switches [87]–[89] are adopted to realize the reconfigurability. However, this mechanism suffers from the tuning discontinuity which limits its flexibility. The integrated filters that incorporate the magnetic materials mentioned above are usually magnetically tunable. In [4], He presented an integrated tunable band-stop filter that achieved a tunability of 70% under a low magnetic field of 400 Oe working in C-band. However, for some higher frequency filter applications, the relatively lossy ferrite has to be adopted and a large magnetic field is required for tunability [83]. Meanwhile, the instrument for applying a magnetic field is usually bulky and power consuming, which makes the magnetically tunable filters an inferior choice. Integrated ME materials offer a possibility to achieve on-chip electric field tunable filter devices. The advantages of ME tuning mechanism are continuous tuning, low power consumption and easily-defined tuning effect range (determined by the size of ME materials). Current efforts are still committed to mitigate the magnetic material performance degradation induced by the deposition or bonding of the piezoelectric phase in ME materials.

In 2015, the first integrated dual E- and H- field tunable band-pass filter was demonstrated in an inverted-L-shape microstrip structure with a multiferroic heterostructure formed by a spin-sprayed NiZn ferrite film and a PMN-PT piezoelectric slab, as shown in Fig. 8(a) [14]. The signal from the input port is transmitted as magnetostatic surface wave (MSSW). The forward and backward wave transmissions happen on bottom and top surface of the ferrite film. The passband frequency of the filter is determined by the dispersion relation of the MSSW. Due to the discrepancy of radiation resistance on the top and bottom surfaces of the ferrite film, a non-reciprocal transmission characteristic can be observed [90], [91]. By ideally rotating the NiZn ferrite film by 45 degrees, the standing wave resonance and the multi-passband are diminished since the reflected wave at the edge of ferrite film is converted to magnetostatic back volume wave (MSBVW) which will decay fast at the filter operating frequency. The detail of the filter operation principle is presented in [92]. As shown in Fig. 8(b), the 15.8 dB difference of S$_{12}$ and S$_{21}$ in band shows the non-reciprocal transmission. The central frequency could be electrically tuned from 2.075 GHz to 2.295 GHz when the out-of-plane electric field rises from 0 kV/cm to 4 kV/cm, as shown in Fig. 8(c), namely an E-field frequency tunability of 55 MHz/(kV/cm). In addition, a tunable central frequency from 3.78 GHz to 5.27 GHz could be realized by increasing the DC magnetic field from 100 Oe to 400 Oe, corresponding to an H-field frequency tunability of about 5 MHz/Oe, as shown in Fig. 8(d).

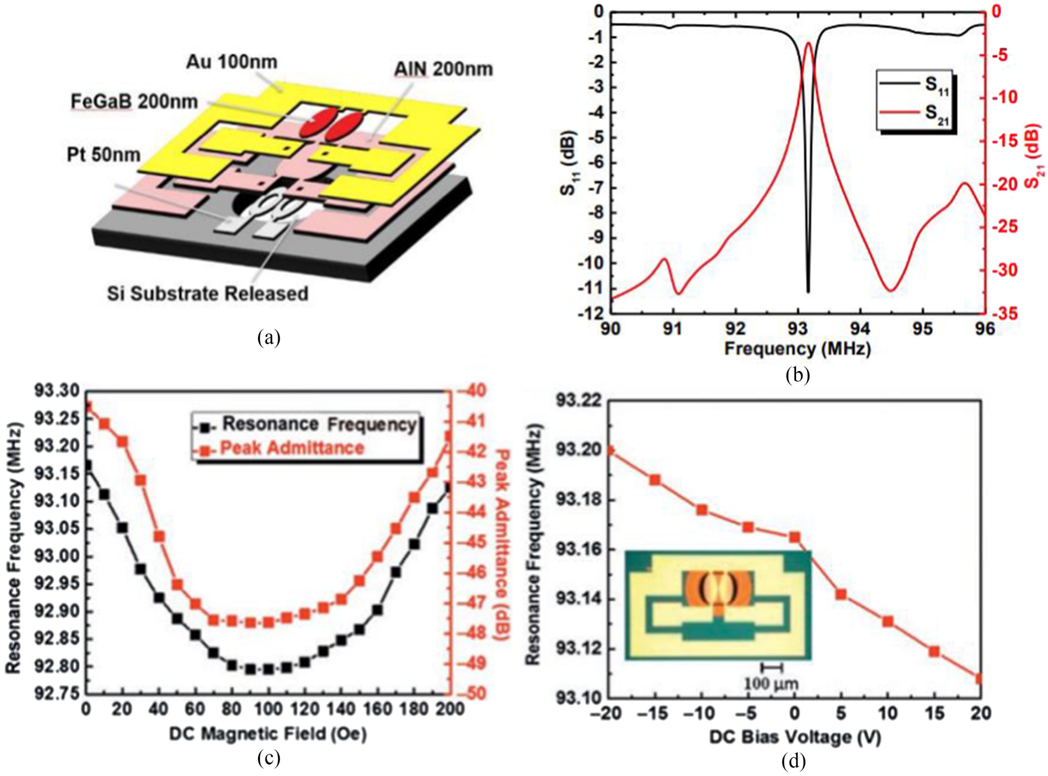

(a)

(b)

(c)

(d)

FIGURE 9. Integrated FeGaB/Al_2O_3/AlN dual E- and H-field tunable ME band-pass filter. (a) Schematics of integrated tunable filter. (b) S_{11} and S_{21} of the tunable filter at zero bias field. (c) Measured resonant frequency as a function of DC magnetic field. (d) Measured resonant frequency as a function of DC voltage across the thickness direction of the AlN film. (Reproduced from [86]).

In 2016, an integrated RF tunable bandpass filter based on two coupled elliptic-shape nano-mechanical resonators with FeGaB/Al_2O_3/AlN multiferroic heterostructure on a bottom Pt electrode were reported [86] and schematically shown in Fig. 9(a). The filter relies on the acoustic wave propagation to achieve signal transmission between the two ports, the two resonators work in the contour mode whose resonance frequency is determined by the width of the coupled structure. The filter exhibited a return loss of -11.2 dB, an insertion loss of 3.4 dB and a quality factor of 252 at the central frequency of 93.165 MHz, as shown in Fig. 9(b). The tunability test showed a H-field frequency tunability of 5 kHz/Oe and an E-field frequency tunability of 2.3 kHz/V, presented in fig. 9(c), (d), respectively. The tunability is realized based on the ΔE effect, where the Young's modulus of FeGaB changes with applied fields.

C. STATE-OF-ART INTEGRATED ME ANTENNAS

Conventional antennas rely on the direct excitation of current or voltage to control the motion of electrons inside resonators for radiation and typically have sizes ranging from one-tenth to one-half of the electromagnetic (EM) wavelength λ_0 [93], [94]. Multiple miniaturization techniques have been applied to design miniature antennas with different structures, such as dipoles, monopoles, slot, Z-type, metamaterial loaded antennas [95]. Electrically small antenna performance is restricted by the Chu–Harrington limit [96]–[99]. The inherent high quality factor (Q-factor) of these antennas limits both the radiation efficiency and operating bandwidth.

The concept of ME antennas was first put forward in [100, 101]. Unlike the conventional antennas that use oscillating charges to induce EM waves, the ME antennas use magnetic dipole moment oscillations that are acoustically actuated at their electromechanical resonance (EMR) rather than the EM wave resonance. Therefore, though there is no proof that the Chu–Harrington limit has been overcome, the antenna dimensions of the mechanical antennas can be decoupled with the wavelength of EM waves. Since the velocity of acoustic waves is orders of magnitude slower than EM waves at the same operation frequency, the application of ME antennas will lead to 1–2 orders of miniaturization in antenna dimension. In addition, ME mechanical antennas based on novel ME composites could maintain a high radiation efficiency, wide bandwidth, low power loss and even high transmission rates and adjustable multiband under appropriate design and nonlinear modulation strategy, which may become an excellent solution to very low frequency (VLF) communication [102], broadband wearable and implantable biomedical devices [103]–[106] and multiband portable devices [107].

The ME antennas consisting of one layer of piezoelectric material and one layer of magnetostrictive material rely on the bulk acoustic wave (BAW) resonator to transfer the dynamic

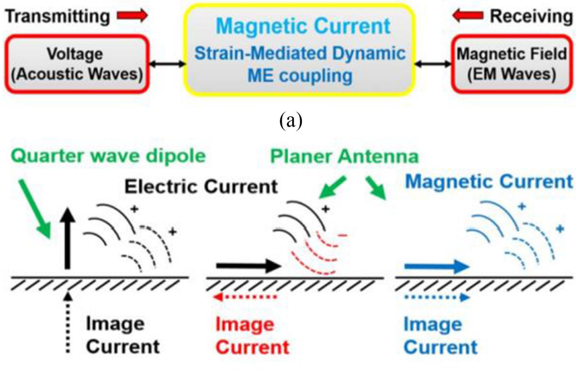

(a)

(b)

FIGURE 10. **(a) Illustration and explanation of the new antenna mechanism. (b) Illustration and explanation of the ground plane effect. (Reproduced from [108]).**

strain across different layers. The illustration of the novel ME antenna mechanism is shown in Fig. 10(a) [108]. On the transmitting side, by applying RF electric field, the mechanical resonance would induce an alternating strain wave/acoustic wave that can be directly transferred to the upper ferromagnetic thin film. The acoustic wave would then induce a dynamic change of the magnetization due to the strong piezomagnetic effect and generate a magnetic current for radiation. Reciprocally, on the receiving side, the RF magnetic field component of the electromagnetic wave can induce an acoustic wave on the ferromagnetic layer. The acoustic wave is then transferred to the piezoelectric layer and converted to the electric voltage output. Different from the cancelling effect of imaging currents in the ground plane of radiation in conventional EM antennas, the usage of magnetic currents for radiation in ME antennas would provide a 3 dB gain enhancement due to in-phase image currents attaching on the ground, as shown in Fig. 10(b). This ground plane immunity property can provide a variety of applications on the metallic surface and the human body which is also considered as a ground plane.

The first batch of ME antennas were fabricated by Nan in 2017, based on laterally-vibrating nano plate resonator (NPR) and vertically-vibrating film bulk acoustic resonator (FBAR) [15]. The ME Antenna with NPR consisted of a rectangular resonating plate with a single-finger bottom Pt electrode and a thin film FeGaB/AlN active resonant heterostructure, as shown in Fig. 11(a). As shown in Fig. 11(c), a high ME coupling coefficient of $\alpha_{ME} = 6$ kVOe^{-1} cm^{-1} can be obtained at EMR frequency $f_{r,NPR}$ of 60.68 MHz without DC bias magnetic field, indicating a strong ME coupling. The strong ME coupling leads to a high electromechanical transduction efficiency, low loss and effective interaction between acoustic resonance and RF magnetic field component of EM waves, which contributes to a high-quality factor Q of 930 and an electromechanical coupling coefficient (k_t^2) of 1.35%, as shown in Fig. 11(b). The ME NPR antenna achieves 1–2 orders of magnitude miniaturization over state-of-the-art compact antennas without performance degradation.

The ME FBAR antenna was composed of a suspended FeGaB/AlN ME circular disk, as shown in Fig. 11(d). Different from ME NPR antennas, the ME FBAR antenna operated at GHz in thickness extensional vibration mode, as shown in Fig. 11(e). The ME FBAR antennas exhibited a peak return loss of 10.26 dB, a Q-factor of 632 and a mechanical resonance frequency of 2.53 GHz. The operating frequency (same as the mechanical resonance frequency) $f_{0,FBAR}$ can be changed by adjusting the thickness T of the ME heterostructure due to the relation $f_{0,FBAR} \propto \frac{1}{T}\sqrt{\frac{E_{eq}}{\rho_{eq}}}$, where T represents the thickness of the FBAR resonator; E_{eq} is the equivalent Young's modulus; ρ_{eq} is the equivalent density of the ME composite. The FBAR antenna achieved an antenna gain of -18 dBi at the resonance frequency of 2.53 GHz based on the measured radiated signal (S_{12}) and received signal (S_{21}), as shown in Fig. 11(f). Compared with the state-of-art conventional compact antennas operating at the same frequency, the dimension of the ME antenna is 1 or 2 orders smaller due to the guided acoustic wave with much lower velocity compared to the EM wave.

The designed and fabricated NPR and FBAR ME antennas could realize different modes of vibration and radiation at both very high frequency (VHF, 60 MHz) and ultra-high frequency (UHF, 2.525 GHz) operation frequency bands. Moreover, the similar microfabrication process of both NPR and FBAR based antennas on the same silicon wafer allows the integration of broadband ME antenna arrays working in the frequency range from tens of MHz (NPR with large lateral dimensions) to tens of GHz (FBAR with thinner AlN thickness) on one chip. These ultra-compact ME antennas serve as the potential candidates for future communication systems, internet of things, wearable antennas, bio-implantable and bio-injectable antennas, smart phones and wireless communication systems.

IV. INTEGRATED MAGNETIC AND MAGNETOELECTRIC FOR SENSING APPLICATIONS

During the past decades, the ultra-sensitive magnetic field sensors were highly demanded and utilized in various field including biomedical applications, geographic detection, electric malfunction diagnosis and information technologies, etc. For practical usage, more figures of merit should be considered, including working bandwidth, temperature stability, linearity, power consumption and cost [109]. Currently the best limit of detection (LOD) of single digit fT/Hz$^{1/2}$ at 1 Hz was achieved by superconducting quantum interference device (SQUID) magnetometer [110]. However, the SQUID requires near-zero working temperature and hence bulky and expensive. Integrated magnetic and magnetoelectric sensors, which take the advantage of its silicon/CMOS compatibility and size suitable for large sensor arrays, have drawn much interest in recent years and notable progresses have been made. The magnetic or magnetoelectric materials integrated in these sensor applications typically have electric or magnetic properties that are sensitive to the external weak

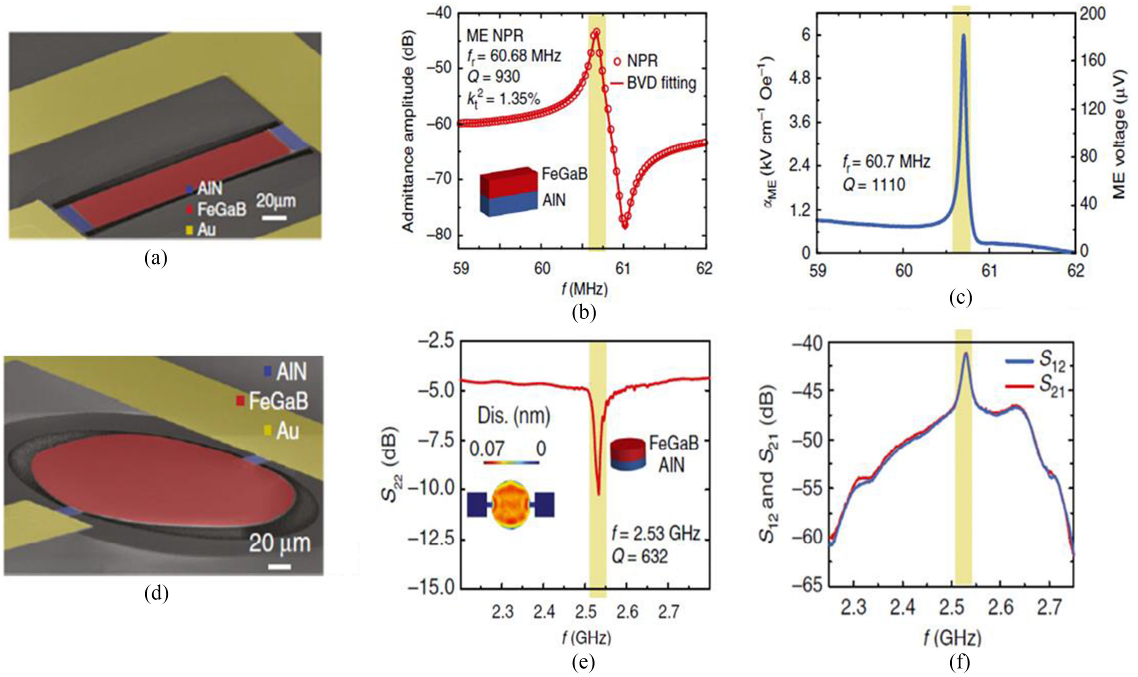

FIGURE 11. Magnetoelectric (ME) nanoplate resonator (NPR) and film bulk acoustic resonator (FBAR) antennas with gigantic ME coupling. ME NPR antenna: (a) Scanning electron microscopy (SEM) images of the fabricated ME NPR antenna. (b) Admittance curve and Butterworth–van Dyke model fitting of the ME NPR. The inset shows the schematic of the cross-section of the ME heterostructure. (c) ME coupling coefficient (left axis) and the induced ME voltage (right axis) versus the frequency of RF magnetic field excitation H_{RF}. FBAR antenna: (d) SEM photo. (e) return loss S_{22} and (f) radiating characteristic (S_{12}) and receiving characteristic (S_{21}) at resonance of the FBAR device. (Reproduced from [15]).

TABLE 4. Integrated Magnetic and Magnetoelectric Devices for Magnetic Field Sensing Applications

Physical Properties or Mechanisms	Devices	References	Key Device Specifications
DME/ΔE effect	ME sensor	[11], [129-131]	f_r=868 Hz, LOD_{ac}=400 fT/Hz$^{1/2}$ [130] f_r=215 MHz, LOD_{dc}=300 pT [131]
High magnetic remanence	Hard magnet-based sensor	[118]	LOD_{ac}=7.2 pT/Hz$^{1/2}$ @2.2 kHz Sensitivity=37.1 KV/T [118]
Magnetoresistance effects	MR sensor	[114], [115], [144], [157]	LOD_{ac}=~3pT/Hz$^{1/2}$ @100Hz Sensitivity=4.9 KV/T [115]

magnetic field, which directly induces a measurable electric output in thin film-based devices, or changes the mechanical properties of the sensor structure in MEMS devices and subsequently the electric output. The prevalent integrated magnetic sensors include ME sensor [11], [111]–[113], magnetoresistance (MR) sensor [114], [115], permanent magnet-based sensor [116]–[120], and fluxgate sensor [121]. In this section, the principle and typical sensor structure of first three types of sensors will be elaborated where the integrated magnetic or magnetoelectric material serves as the sensing element. In the fluxgate sensors, the magnetic material serves as core which shares the similar function as integrated inductors and transformers. A cross comparison of the sensors discussed in this work is given in Table 4.

A. INTEGRATED ME SENSOR

The two-phase ME composite that consists of a piezoelectric/electrostrictive phase and a magnetostrictive phase is capable to directly convert the magnetic moment to the electric polarization and subsequently the output voltage through the mechanical coupling between the two phases, which enables the possibility of its sensing application. The sensing performance of the composite is majorly determined by 1). The material properties of both phases including the piezoelectric and magnetostrictive constant, stiffness, dielectric constant and permeability. 2). The mechanical structure issues including the volume and thickness ratio of two phases, the mechanical coupling condition. 3). The operating mode which determines the mechanical deformation and polarization directions [122].

Earlier works [123], [124] on ME sensors focused on forming the bulk ME laminate structure by epoxy bonding to detect the external weak magnetic field thorough direct ME coupling, where a strain induced by the magnetic field in magnetostrictive phase is transferred to piezoelectric phase and reflected at the electric output. However, the major drawback of this scheme is the narrow detectable bandwidth considering the mechanical resonance characteristic of the sensor and the high flicker noise in the low frequency range. A DC bias field is also needed for optimizing the ME coupling coefficient in the measurement frequency range. Moreover, the epoxy glued ME sensors suffer from the temperature stability and device fatigue issues. Some efforts have been put into optimizing the sensor configuration and structure to achieve higher sensitivity by optimizing sensor geometry [125], improving the lamination process [126], performing a differential sensor configuration [127] and improving the output signal processing [128].

To tackle the above-mentioned bonding issues, thin-film technologies are adopted to deposit the two phases in the ME composite, which enables a more desirable bonding condition and hence improves the ME coupling coefficient. The mostly used soft magnetic materials for magnetostrictive phase include FeGa [129], FeCoSiB [130] and FeGaB [131], while the piezoelectric phase is typically AlN [132], PZT [129] and PVDF [133]. The frequency conversion technique was first proposed by Jahns [134] and was widely adopted [135], [136] to expand the operating frequency range of the ME sensor, particularly in the low frequency regime. The technique utilizes the non-linear magnetostrictive response and converts the low frequency magnetic field component to a frequency-mixing component close to the resonance by applying a modulation magnetic field at resonance frequency. The frequency mixing component intensity was utilized to determine the weak magnetic field under detect.

Integrated ME sensors has its unique advantage in forming the well-arranged sensor array, compatibility of CMOS process and power efficiency. Currently, the principle of integrated ME sensor includes ΔE effect and the direct ME coupling. Like the bulk ME sensors, the integrated ME sensor that relies on the direct ME coupling can only detect the AC magnetic field with frequency close to its resonance. An external DC bias magnetic field is also required to optimize the ME coupling and LOD. The ΔE integrated ME sensor, on the other hand, utilizes the ΔE effect in magnetostrictive phase, where the Young's modulus changes with the magnetic field under detect. The mechanical characteristic of the sensor is then altered and can be detected by optical detection of the deflection [111], close-loop measurement of the resonance frequency [112], open-loop measurement for sensor admittance [131] and direct output voltage readout through a directional coupler [113]. The ΔE ME sensor provides the possibility for wideband operation and low frequency/DC magnetic field detection. The two types of integrated sensors are exemplified below in detail to illustrate the device structures and working principles.

In [11], Su proposed to use AlScN/FeCoSiB laminate ME structure for sensing application based on direct ME coupling. The simplified sensor structure is shown in Fig. 12(a), where a 1 μm thick AlScN layer and a 2 μm thick FeCoSiB layer were deposited on a poly-silicon cantilever. The Mo top electrode and the Ti/Pt bottom electrode are not shown in the schematic. The polysilicon cantilever structure was obtained through a TMAH etching process. The as-fabricated sensor was packaged and mounted on the test board shown in Fig. 12(b) with a wafer-level transient-liquid-phase process. A series of AlN based sensors were also fabricated for performance comparison. Fig. 12(c) demonstrates the ME coefficient measurement results of sensors with different piezoelectric phase. The AlScN material provides a factor of 2 improvement on the ME coefficient compared to its AlN counterpart, reached a value of 1580 V/cm·Oe at 8185 Hz. The electric noise spectrums of both sensors are given in Fig. 12(d) with the reference audio noise. The peak position that appears in the spectrum coincides with that of ME coefficient. The LOD of each sensor was calculated by finding the ratio of the ME coefficient to the electric noise density at resonance. The best LOD achieved was 55 $\mathrm{pT/Hz^{1/2}}$. It was also shown that despite the increase in ME coefficient for AlScN based sensor, the LOD did not get a similar boost at resonance. This was caused by the scaling up thermomechanical noise with larger sensor deflection in AlScN based sensor. It was also reported the working frequency of such sensors is tunable by an external applied DC electric field to the piezoelectric phase.

In 2013, Nan [131] reported a 215 MHz NEMS resonator to detect DC magnetic field based on ΔE effect. The structure of the resonator is shown in Fig. 13(a). The resonator adopted an $\mathrm{AlN/(FeGaB/Al_2O_3)\times 10}$ ME heterostructure with interdigital Pt electrode at bottom. The FeGaB soft magnetic multilayer has lower eddy current loss compared with one single layer and the interdigital electrode with designed pitch width drives the resonator in extension vibration mode. With fixing pitch width and equivalent density, the resonance frequency of the sensor is purely determined by the effective Young's modules, which is affected by the DC magnetic field under detect due to the ΔE effect. Fig. 13(b) shows the admittance spectrum under different applied DC magnetic field, presenting the effect of changing Young's modules electrically. The peak admittance and quality factor Q under different applied DC magnetic field is plotted in Fig. 13(c). The quality factor has a minimum at 15 Oe, which is caused by the variation of the magnetic domain wall state and the corresponding loss. With large magnetic field applied, the magnetic domain wall is eliminated, reducing the magnetic loss, and hence increasing the quality factor. To test the sensing capability, the resonator was biased under 5 Oe DC magnetic field where the resonance frequency was at the most sensitive point to the applied field. The resonator was then excited at a single frequency for admittance measurement under a superimposed tiny DC field as low as 50 pT. The measurement result is shown in Fig. 13(d), where a 300 pT LOD was determined. The 10-layer $\mathrm{FeGaB/Al_2O_3}$ magnetostrictive material also showed a

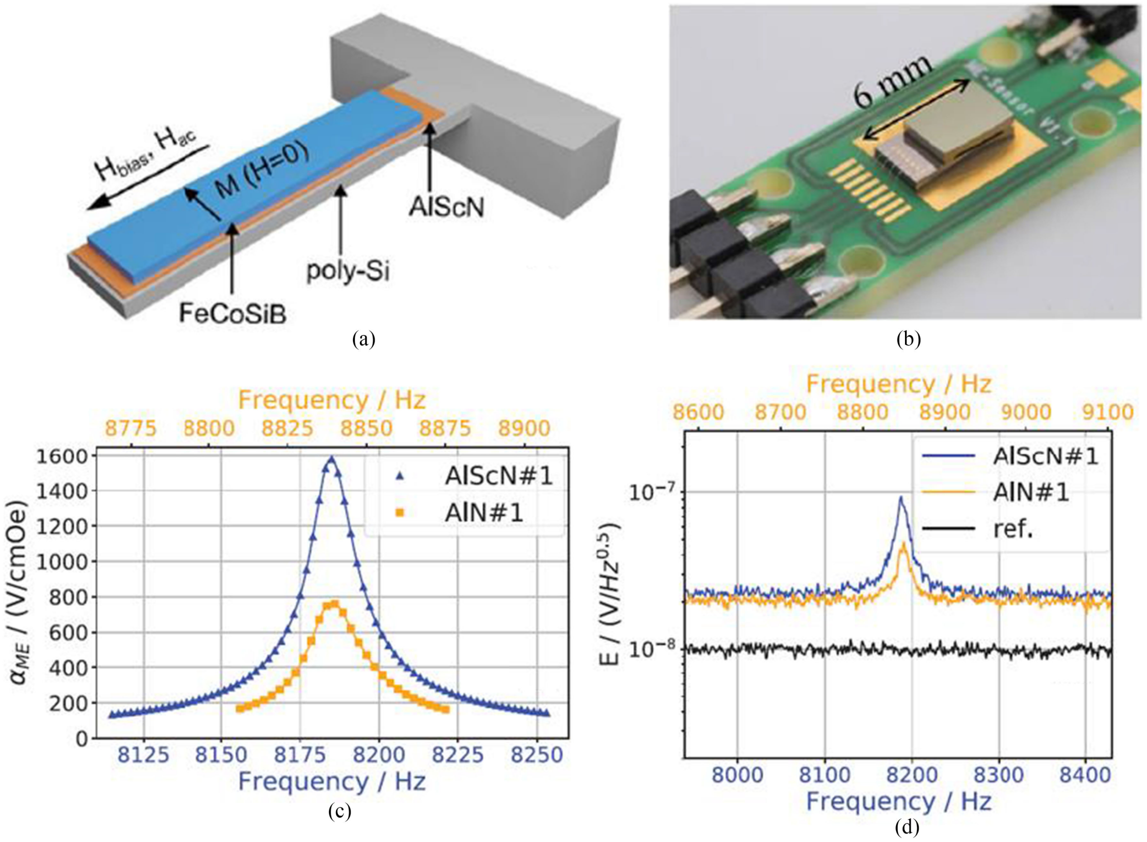

(a) (b) (c) (d)

FIGURE 12. (a) Schematic of the MEMS AlScN resonant magnetoelectric sensor. (b) photograph of the packaged ME chip on a test board. (c) Measured ME coefficient αME of AlScN and AlN based ME sensors at their mechanical resonance. (d) Voltage noise density spectra for AlScN (blue) and AlN (orange) based ME sensors as well as a reference channel (black). (Reproduced from [11]).

self-bias performance which offered a LOD of 600 pT with no DC magnetic field bias.

B. INTEGRATED PERMANENT MAGNET-BASED SENSOR

The permanent magnets represent a group of ferromagnetic or ferrimagnetic materials that exhibit strong magnetization after the removal of external field. The most commonly used permanent hard magnet materials include ferrites, transition metal alloys and rare-earth alloys [137]. Unlike the bulk permanent magnets fabrication, the silicon compatible integration of permanent magnets suffers the following difficulties and challenges: 1). The harsh fabrication conditions including the high temperature and pressure are not suitable for on-chip process; 2). The traditional deposition methods including electrodeposition [138], magnetron sputtering [139] and pulsed laser deposition (PLD) [140] typically generate thin film material with the thickness in the range of nanometer to micrometer, which fairly limits the sample performance; 3). The wafer-level patterning of the as-deposited permanent magnetic material may be hard to conduct or require specific etching process that would damage the pre-exist structures. Numerous efforts have been put into developing new powder-based on-chip permanent magnet fabrication methodologies to overcome these challenges including spin casting/screen printing [141], dry-packing [142] and 3-dimensional (3D)-printing [143]. The Ongoing research on powder-based permanent magnet integration is focusing on improving the packing density and the micro-structure of the magnetic powder which is essential to the magnet performance.

With the advance of fabrication technique, the integrated permanent magnet is utilized and serves as a sensing part that responds to the external magnetic field under detect. The mechanical force or torque generated is transferred to piezoelectric phase and converted to electric outputs for readout [116]–[118]. Compared to optical detection [119], [120], the piezoelectric readout scheme does not need the optical generation, coupling and collimation instrument, which is favorable for outdoor detection in harsh environment. In 2019, Niekiel [118] reported a fully integrated permanent magnet-based sensor that adopted the cantilever structure. The schematic of sensor working principle and the structure are shown in Fig. 14(a) and (b) respectively. When the integrated NdFeB magnet was magnetized along the vertical direction and with the magnetic field under detect applied along the horizontal direction, a torque can be generated and drive the cantilever whose deflection was monitored by the AlN piezoelectric layer. Two types of devices with different cantilever length are shown in Fig. 14(c), where the electrodes were wire-bonded to a PCB for the measurement. The sensitivity frequency spectrums are

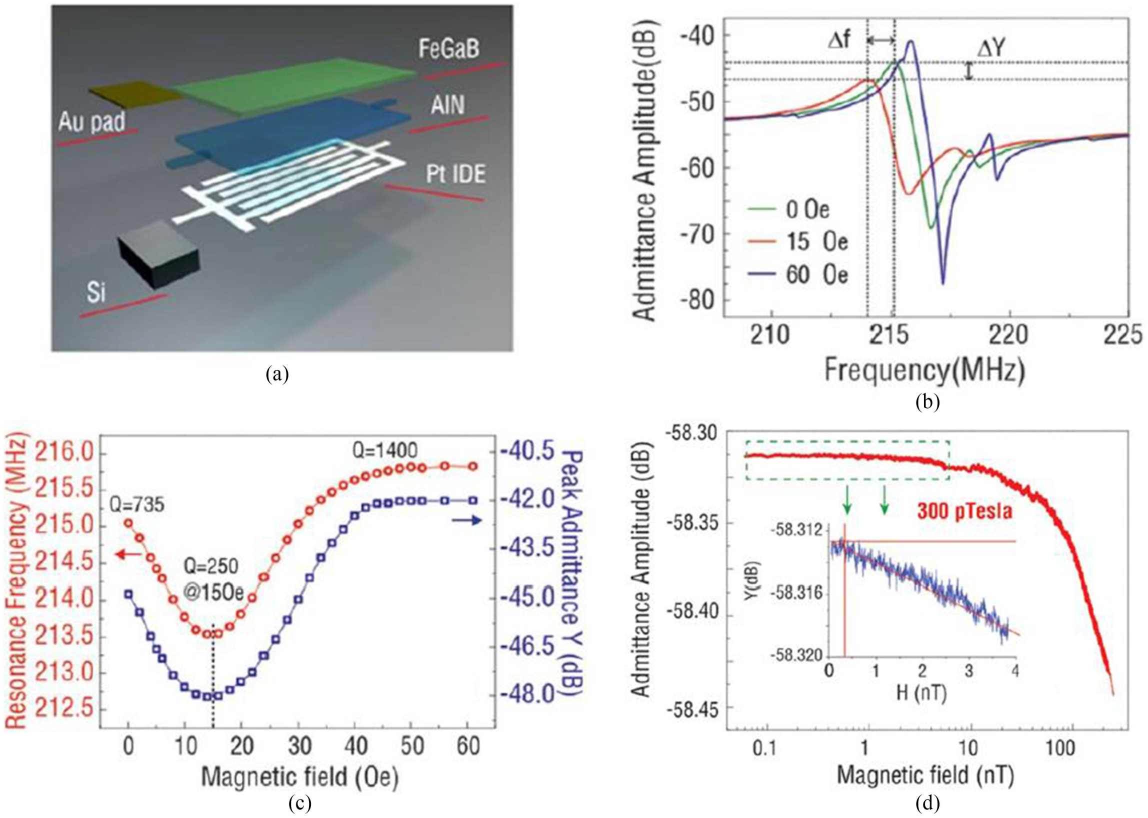

(a) (b) (c) (d)

FIGURE 13. **(a) Schematic of NEMS ME resonator. (b) Admittance curves of the NEMS sensor at various bias DC magnetic fields. (c) Resonance frequency and admittance amplitude at the resonance frequency as a function of DC magnetic field. (d) Sensitivity measurement results under 5 Oe DC magnetic field bias. (Reproduced from [131]).**

plotted in Fig. 14(d). The peak sensitivity of sensor 1 and 2 are 34.6 kV/T and 37.1 kV/T, respectively. The sensors showed a high quality factor oscillator characteristic which boosted the sensitivity in band. The vertically magnetizing permanent magnet configuration also offers superior sensitivity performance compared to its horizontal counterparts which rely on the magnetic field gradient for sensing. To determine the LOD of the sensors, the electric noise density was measured and divided by the sensitivity, it is shown in fig. 14(e) that the LOD at resonance is 7.2 pT/Hz$^{1/2}$ for sensor 1 and 7.3 pT/Hz$^{1/2}$ for sensor 2.

C. INTEGRATED MAGNETORESISTVE MATERIALS AND SENSORS

Magnetoresistance effect refers to the effect that the resistance of the thin film material varies under the external magnetic field. The 3 major categories of MR including anisotropic magnetoresistance (AMR), giant magnetoresistance (GMR) and tunnel magnetoresistance (TMR). The AMR is attributed to the anisotropic differences in the scattering of s electrons off d electrons resulting from spin-orbit interaction [144] and always happens in the transition metal and transition metal alloys [145]. The GMR and TMR effect rely on the spin-dependent electronic transport. All the MR effects have been utilized for sensing applications and commercialized products are available. Typically, the MR sensors are used in magnetic read head in magnetic hard disk drive, automotive and consumer electronics including current leakage detection, positioning, and biotechnology, etc [146]. The noise energy spectrums of commercially available MR sensor products are shown in Fig. 15 [147]. Note the term 'detectivity' as the Y-axis name in the plot refers to the noise floor level . The sensor types corresponding to the product part numbers are marked in the caption of the plot. It is shown among all the MR sensors, AMR sensor has lowest noise performance in the low frequency range. However, due to the physical nature of these MR effect, the AMR have the lowest magnetoresistance change, namely around 2%−4% [144], compared to ∼10% in GMR device under low magnetic field, and as high as 220% [148], [149] to 600% [150] in TMR structures.

A typical GMR device consists of two ferromagnetic layers with a non-magnetic conductive layer in between, whereas for the TMR case, the non-magnetic layer in between is a semiconductor or an isolator layer and the electron travels through the layered structure by tunneling effect. The two ferromagnetic layers are deposited to a designed thickness such that a spontaneous anti-parallelly aligned magnetization is achieved in these two layers. The external applied field forces the magnetization in both ferromagnetic layers, which subsequently decreases the overall resistance of the structure due to the spin-dependent electron transport. The theory of the spin-induced electric difference is elaborated by two current

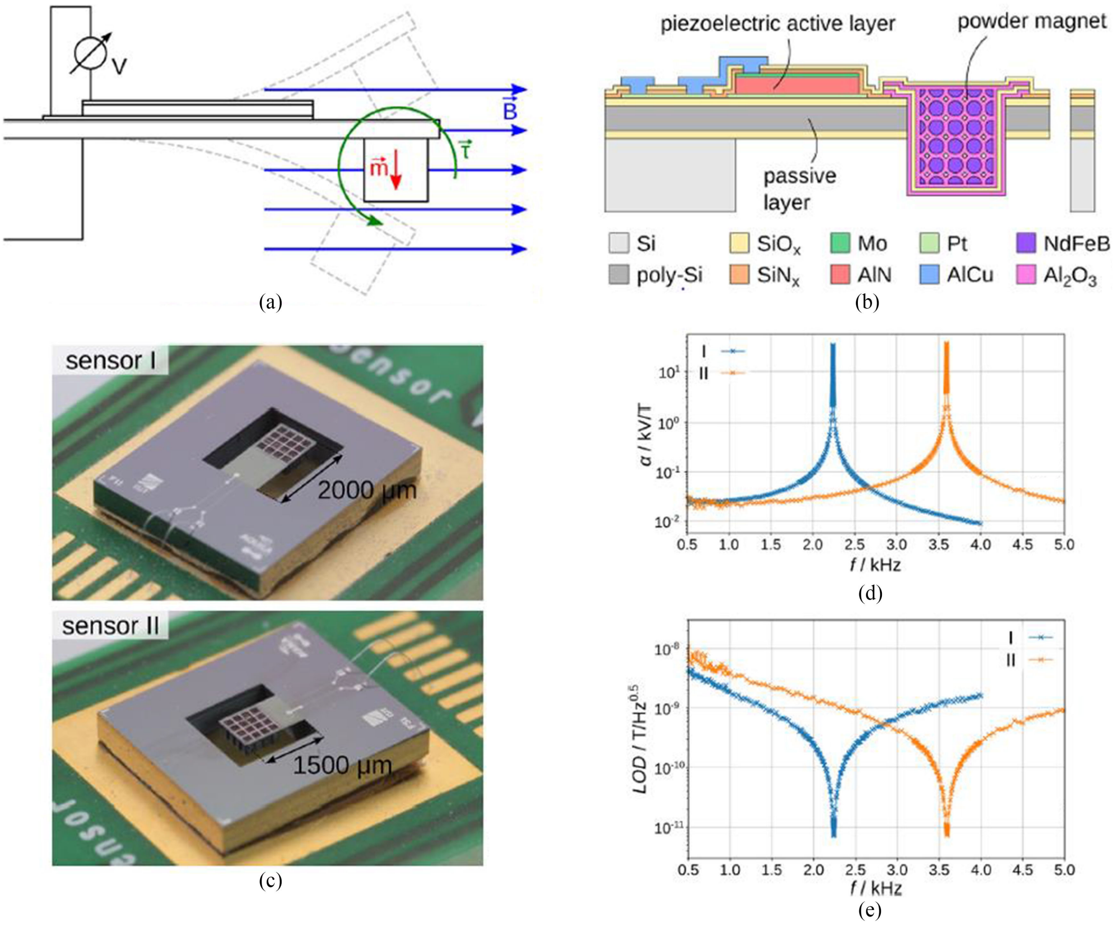

(a) (b) (c) (d) (e)

FIGURE 14. **(a) Working principle of the integrated permanent magnet-based sensor. (b) Cross-sectional view of the sensor structure. (c) Images of the sensors mounted on PCB. (d) Frequency dependency of sensor sensitivity. (e) Frequency dependency of limit of detection. (Reproduced from [118]).**

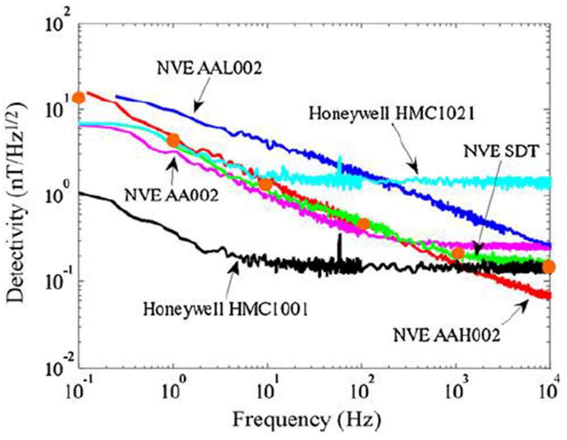

FIGURE 15. **The noise energy density of commercially available MR sensors, in which NVE AAL002 is GMR sensor; NVE SDT is TMR sensor; Honeywell HMC1001 is AMR sensor. (Reproduced from [141]).**

models proposed by Mott [151]. Since the first discovery of GMR effect by Fert in 1988 using Fe/Cr superlattice [152], numerous efforts have been put into improving the magnetoresistance changing ratio of GMR/TMR thin film layered structure. In 1991, Dieny [153] proposed a structure named spin valve where the magnetization of one of ferromagnetic layers mentioned above was pined by an anti-ferromagnetic layer (typically Mn alloy) adjacent to it through the spin interaction, which overcame the issue that the previous structures were only sensitive to high magnetic field. To further reduce the field required to reverse the magnetization direction in ferromagnetic layers, a synthetic anti-ferromagnetic layer structure that consists of two ferromagnetic layer (typically FeCo alloy) and a coupling Ru layer was proposed by Parkin [154]. It was found then by Parkin [155] introducing a Co-rich alloy layer between the ferromagnetic layer and spacer of simple GMR structure doubled the MR changing amount. The TMR effect under room temperature was first demonstrated by Moodera [156] in FeCo/Al$_2$O$_3$/Co structure where Al$_2$O$_3$ acted as insulting barrier for tunneling effect. The MgO isolation layer was also widely used since then.

Although the GMR/TMR effect offers great potential in sensing application thanks to their large MR change under external magnetic field, it has some major drawbacks including the non-linear response and hysteresis characteristic. Typically, a DC magnetic bias generated by the Helmholtz coils or permanent magnet can mitigate the issue [157]. Differential [114] and bridge [115] sensor configurations have

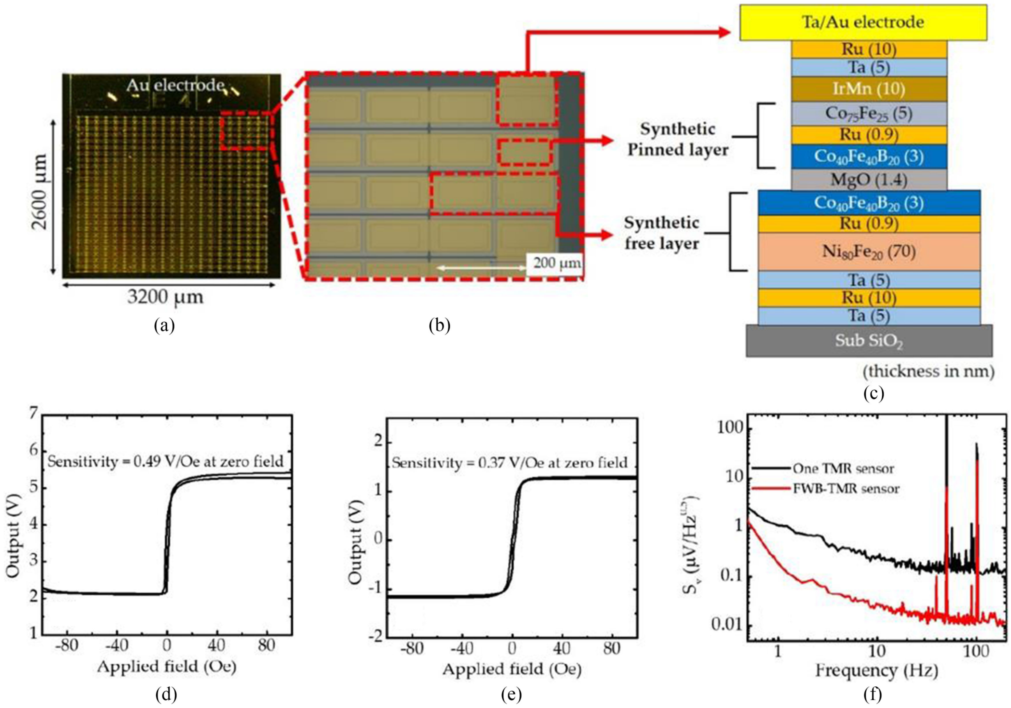

FIGURE 16. **(a,b) Microscopy image of a serial TMR sensor. (c) Stacking structure of TMR sensor. (d) Outputs for one serial TMR sensor and (e) four serial TMR sensors connected in a full Wheatstone bridge circuit at room temperature. (f) Noise spectrum of one serial TMR sensor and four serial TMR sensors connected in a full Wheatstone bridge circuit. (Reproduced from [115]).**

also been adopted to improve the sensitivity and diminish the noise.

In [115], Jin fabricated and utilized the on-chip TMR sensors for magnetic field leakage detection. The optical images of the as-fabricated devices connected in series are shown in Fig. 16(a) and (b), and the layered sensor structure with constituent and thicknesses in nanometer of each layer is schematically shown in Fig. 16(c). The TMR sensor adopted synthetic ferromagnetic layers and the magnetization of the upper one was pinned by IrMn material. The MgO layer was adopted as tunneling barrier. The magnetic field sensitivity was tested for one serial TMR sensor and four serial TMR sensors connected in Wheatstone bridge configuration are shown in Fig. 16(d) and (e), respectively. The sensitivity of one sensor was 0.49 V/Oe and that of the 4-element bridge is 0.37 V/Oe at zero field. Although some compromises were made on the sensitivity, the 4-element bridge showed better linear range by 6 Oe and nearly one order lower intensity in noise energy spectrum which is shown in Fig. 16(f).

V. CONCLUSION

During the past several decades, integrated magnetic and magnetoelectric materials are widely utilized and enabling high-efficiency, compact and tunable on-chip devices, which shows a bright future for power, RF, microwave and sensing applications. Ongoing research is focusing on controlling the magnetic damping to either achieving high efficiency in magnetostatic wave based high frequency devices, or to control the ferromagnetic behavior and consequently domain wall dynamics and spin transfer torque switching [158]. The integration of highly dense hard magnet has long been another difficulty for the community which is in the needs of more versatile fabrication methodologies with accurate positioning and definable pattern on silicon. As for the integrated magnetoelectric, surely the materials with high piezoelectric and magnetostrictive coefficients are highly demanded for stronger ME coupling. The stress elimination in the two-phase ME composite is also desirable to optimize the device performance, which requires deposition condition, releasing process control and even the post-fabrication annealing. Some researchers also commit to get better understanding on physical basis of strain-mediated magnetization and the radiation mechanism of ME antennas. For practical applications, biomedical stimulus and sensing incorporating the NEMS ME sensors and antennas has become a research hotspot. Considering the miniaturization brought by the novel ME devices on transmitting and sensing devices, they are good candidates for invasive probing and non-invasive wearable products in healthcare domain.

REFERENCES

[1] H. Szymczak, "Magnetic materials and applications," in *Encyclopedia of Condensed Matter Physics*. Waltham, MA, USA: Academic Press, 2005, pp. 204–211.

[2] A. Haldar, D. Kumar, and A. O. Adeyeye, "A reconfigurable waveguide for energy-efficient transmission and local manipulation of information in a nanomagnetic device," *Nature Nanotechnol.*, vol. 11, no. 5, pp. 437–443, 2016.

[3] Y. Gao *et al.*, " Significantly enhanced inductance and quality factor of GHz integrated magnetic solenoid inductors with FeGaB/Al_2O_3

multilayer films," *IEEE Trans. Electron Devices*, vol. 61, no. 5, pp. 1470–1476, May 2014.

[4] Y. He *et al.*, "Integrated tunable bandstop filter using self-biased FeGaB/Al_2O_3 multilayer thin film," *IEEE Trans. Magn.*, vol. 54, no. 9, pp. 1–4, Sep. 2018.

[5] W. Che, E. K. N. Yung, K. Wu, and X. Nie, "Design investigation on millimeter-wave ferrite phase shifter in substrate integrated waveguide," *Progr. Electromagn. Res.*, vol. 45, pp. 263–275, 2004.

[6] R. Zand, A. Roohi, and R. F. DeMara, "Energy-efficient and process-variation-resilient write circuit schemes for spin hall effect MRAM device," *IEEE Trans. Very Large Scale Integr. (VLSI) Syst.*, vol. 25, no. 9, pp. 2394–2401, Sep. 2017.

[7] D. E. Nikonov and G. I. Bourianoff, "Spin gain transistor in ferromagnetic semiconductors-the semiconductor Bloch-equations approach," *IEEE Trans. Nanotechnol.*, vol. 4, no. 2, pp. 206–214, Mar. 2005.

[8] S. Kaka, M. R. Pufall, W. H. Rippard, T. J. Silva, S. E. Russek, and J. A. Katine, "Mutual phase-locking of microwave spin torque nano-oscillators," *Nature*, vol. 437, no. 7057, pp. 389–392, 2005.

[9] S. Gupta, P. Bhatter, and V. Kakkar, "Point-of-care detection of tuberculosis using magnetoresistive biosensing chip," *Tuberculosis*, vol. 127, 2021, Art. no. 102055.

[10] N. A. Spaldin and M. Fiebig, "The renaissance of magnetoelectric multiferroics," *Science*, vol. 309, no. 5733, pp. 391–392, 2005.

[11] J. Su *et al.*, "AlScN-based MEMS magnetoelectric sensor," *Appl. Phys. Lett.*, vol. 117, no. 13, 2020, Art. no. 132903.

[12] S. K. Ghosh *et al.*, "Rollable magnetoelectric energy harvester as a wireless IoT sensor," *ACS Sustain. Chem. Eng.*, vol. 8, no. 2, 2019, pp. 864–873.

[13] H. Chen *et al.*, "Integrated tunable magnetoelectric RF inductors," *IEEE Trans. Microw. Theory Techn.*, vol. 68, no. 3, 951–963, Mar. 2020.

[14] H. Lin *et al.*, "Integrated non-reciprocal dual H- and E-field tunable bandpass filter with ultra-wideband isolation," in *Proc. IEEE MTT-S Int. Microw. Symp.*, Phoenix, AZ, USA, May 2015, pp. 1–4.

[15] T. Nan *et al.*, "Acoustically actuated ultra-compact NEMS magnetoelectric antennas," *Nature Commun.*, vol. 8, 2017, Art. no. 296.

[16] I. E. Dzyaloshinskii, "On the magneto-electrical effects in antiferromagnets," *Sov. Phys. JETP*, vol. 10, pp. 628–629, 1960.

[17] N. A. Hill, "Why are there so few magnetic ferroelectrics?,"*J. Phys. Chem. B*, vol. 104, no. 29, pp. 6694–6709, 2000.

[18] X. Liang *et al.*, "A review of thin-film magnetoelastic materials for magnetoelectric applications," *Sensors*, vol. 20, no. 5, 2020, Art. no.1532.

[19] M. M. Vopson, Y. K. Fetisov, G. Caruntu, and G. Srinivasan, "Measurement techniques of the magneto-electric coupling in multiferroics," *Materials*, vol. 10, no. 8, 2017, Art. no. 963.

[20] S. Dong, J. Zhai, J. Li, and D. Viehland, "Near-ideal magnetoelectricity in high-permeability magnetostrictive/piezofiber laminates with a (2-1) connectivity," *Appl. Phys. Lett.*, vol. 89, no. 25, 2006, Art. no. 252904.

[21] J. Lou, M. Liu, D. Reed, Y. Ren, and N. X. Sun, "Giant electric field tuning of magnetism in novel multiferroic FeGaB/lead zinc niobate–lead titanate (PZN-PT) heterostructures," *Adv. Mater.*, vol. 21, no. 46, pp. 4711–4715, 2009.

[22] M. Liu *et al.*, "Giant electric field tuning of magnetic properties in multiferroic ferrite/ferroelectric heterostructures," *Adv. Funct. Mater.*, vol. 19, no. 11, pp. 1826–1831, 2009.

[23] M. Liu, S. Li, O. Obi, J. Lou, S. Rand, and N. X. Sun, "Electric field modulation of magnetoresistance in multiferroic heterostructures for ultralow power electronics," *Appl. Phys. Lett.*, vol. 98, no. 22, 2011, Art. no. 222509.

[24] J. M. Hu, Z. Li, L. Q. Chen, and C. W. Nan, "Design of a voltage-controlled magnetic random access memory based on anisotropic magnetoresistance in a single magnetic layer," *Adv. Mater.*, vol. 24, no. 21, pp. 2869–2873, 2012.

[25] J. H. Griffiths, "Anomalous high-frequency resistance of ferromagnetic metals," *Nature*, vol. 158, no. 4019, pp. 670–671, 1946.

[26] C. Kittel, "Ferromagnetic resonance," *J. Phys. Radium*, vol. 12, no. 3, pp. 291–302, 1951.

[27] N. X. Sun and G. Srinivasan, *Voltage Control of Magnetism in Multiferroic Heterostructures and Devices*. Singapore: World Scientific, vol. 2, no. 3, 2012, Art. no. 1240004.

[28] D. Berlincourt, H. H. A. Krueger, and C. Near "Technical publication TP-226, properties of piezoelectricity ceramics," *Morgan Electro Ceramics*, vol. 12, 2003.

[29] J. Erhart, P. Půlpán, and M. Pustka, *Piezoelectric Ceramic Resonators*. Cham, Switzerland: Springer, 2017.

[30] C. Tu *et al.*, "Mechanical-resonance-enhanced thin-film magnetoelectric heterostructures for magnetometers, mechanical antennas, tunable RF inductors, and filters," *Materials*, vol. 12, no. 14, 2019, Art. no. 2259.

[31] K. Tsubouchi; K. Sugai, and N. Mikoshiba, "AlN material constants evaluation and SAW properties on AlN/Al_2O_3 and AlN/Si," in *Proc. Ultrason. Symp.*, Chicago, IL, USA, Oct. 1981, pp. 375–380.

[32] M.-A. Dubois, and P. Muralt, "Properties of aluminum nitride thin films for piezoelectric transducers and microwave filter applications," *Appl. Phys. Lett.*, vol. 74, pp. 3032–3034, 1999.

[33] J. - L. Sanchez-Rojas *et al.*, "Advanced determination of piezoelectric properties of AlN thin films on silicon substrates," in *Proc. IEEE Ultrason. Symp.*, Beijing, China, Nov. 2008, pp. 903–906.

[34] L. C. Lim, K. K. Rajan, and J. Jin, "Characterization of flux-grown PZN-PT single crystals for high-performance piezo devices," *IEEE Trans. Ultrason. Ferroelectr. Freq. Control*, vol. 54, no. 12, pp. 2474–2478, Dec. 2007.

[35] P. Han, W. Yan, J. Tian, X. Huang, and H. Pan, "Cut directions for the optimization of piezoelectric coefficients of lead magnesium niobate–lead titanate ferroelectric crystals," *Appl. Phys. Lett.*, vol. 86, no. 5, 2005, Art. no. 052902.

[36] K. Uchino, *Advanced Piezoelectric Materials: Science and Technology*. Sawston, U.K.: Woodhead, 2017.

[37] Z. Yang and J. Zu, "Comparison of PZN-PT, PMN-PT single crystals and PZT ceramic for vibration energy harvesting," *Energy Convers. Manage.*, vol. 122, pp. 321–329, 2016.

[38] G. Engdahl and I. D. Mayergoyz, *Handbook of Giant Magnetostrictive Materials*. New York, NY, USA: Academic, 2000.

[39] A. E. Clark, M. Wun-Fogle, J. B. Restorff, and T. A. Lograsso, "Magnetostrictive properties of Galfenol alloys under compressive stress," *Mater. Trans.*, vol. 43, no. 5, pp. 881–886, 2002.

[40] N. Srisukhumbowornchai and S. Guruswamy, "Large magnetostriction in directionally solidified FeGa and FeGaAl alloys," *J. Appl. Phys.*, vol. 90, no. 11, pp. 5680–5688, Nov. 2001.

[41] J. Lou, R. E. Insignares, Z. Cai, K. S. Ziemer, M. Liu and N. X. Sun, "Soft magnetism, magnetostriction, and microwave properties of FeGaB thin films," *Appl. Phys. Lett.*, vol. 91, no. 18, pp. 182–504, Oct. 2007.

[42] H. Greve, E. Woltermann, H.-J. Quenzer, B. Wagner, and E. Quandt, "Giant magnetoelectric coeffcients in (Fe90Co10)78 Si12 B10-AlN thin film composites,"*Appl. Phys. Lett.*, vol. 96, 2010, Art. no. 182501.

[43] Z. Chu *et al.*, "Enhanced resonance magnetoelectric coupling in (1-1) connectivity composites,"*Adv. Mater.*, vol. 29, 2017, Art. no. 1606022.

[44] M. Liu *et al.*, "Electrically induced enormous magnetic anisotropy in Terfenol-D/lead zinc niobate-lead titanate multiferroic heterostructures," *J. Appl. Phys.*, vol. 112, no. 6, 2012, Art. no. 063917.

[45] A. Butera, J. Gómez, J. L. Weston, and J. A. Barnard, "Growth and magnetic characterization of epitaxial Fe 81 Ga 19/MgO (100) thin films," *J. Appl. Phys.*, vol. 98, no. 3, 2005, Art. no. 033901.

[46] C. L. Platt, N. K. Minor, and T. J. Klemmer, "Magnetic and structural properties of FeCoB thin films," *IEEE Trans. Magn.*, vol. 37, no. 4, pp. 2302–2304, Apr. 2001.

[47] I. Kim, J. Kim, K. H. Kim, and M. Yamaguchi, "Effects of boron contents on magnetic properties of Fe-Co-B thin films," *IEEE Trans. Magn.*, vol. 40, no. 4, pp. 2706–2708, Apr. 2004.

[48] J. Lou, R. E. Insignares, Z. Cai, K. S. Ziemer, M. Liu, and N. X. Sun, "Soft magnetism, magnetostriction, and microwave properties of FeGaB thin films," *Appl. Phys. Lett.*, vol. 91, no. 18, 2007, p.182504.

[49] C. Dong *et al.*, "Characterization of magnetomechanical properties in FeGaB thin films," *Appl. Phys. Lett.*, vol. 113, no. 26, 2018, Art. no. 262401.

[50] Z. Chu, M. PourhosseiniAsl, and S. Dong, "Review of multi-layered magnetoelectric composite materials and devices applications," *J. Phys. D, Appl. Phys.*, vol. 51, no. 24, 2018, Art. no. 243001.

[51] W. Ling, C. Xiaoning, X. Hang, H. Wenmei, W. Bowen, and Y. Zeyu, "Frequency-dependent complex magnetic permeability and magnetic losses of Fe-Ga alloy," in *Proc. IEEE 20th Int. Conf. Elect. Machines Syst.*, Aug. 2017, pp. 1–5.

[52] Z. Zhang *et al.*, "Coupling of magneto-strictive FeGa film with single-crystal diamond MEMS resonator for high-reliability magnetic sensing at high temperatures," *Mater. Res. Lett.*, vol. 8, no. 5, pp. 180–186, 2020.

[53] X. Wang *et al.*, "Size-dependent magnetic properties of FeGaB/Al_2O_3 multilayer micro-islands," *Phys. Lett. A*, vol. 382, no. 23, pp. 1505–1508, 2018.

[54] F. Q. Xiao, M. G. Han, H. P. Lu, L. Zhang, E. Li, and L. J. Deng, "Out-of-plane magnetic anisotropy and microwave permeability of magnetoelastic FeCoSiB amorphous thin films," *J. Electron. Sci. Technol.*, vol. 5, no. 3, pp. 226–229, 2007.

[55] E. J. Yun, M. Jung, C. I. Cheon, and H. G. Nam, "Microfabrication and characteristics of low-power high-performance magnetic thin-film transformers," *IEEE Trans. Magn.*, vol. 40, no. 1, pp. 65–70, Jan. 2004.

[56] B. M. Mundotiya, D. Dinulovic, L. Rissing, and M. C. Wurz, "Fabrication and characterization of a Ni-Fe-W core microtransformer for high-Frequency power applications," *Sens. Actuators A, Phys.*, vol. 267, pp. 42–47, 2017.

[57] S. G. Mariappan, A. Moazenzadeh, and U. Wallrabe, "Polymer magnetic composite core based microcoils and microtransformers for very high frequency power applications," *Micromachines*, vol. 7, no. 4, 2016, Art. no. 60.

[58] X. Wang *et al.*, "A novel NiZn ferrite integrated magnetic solenoid inductor with a high quality factor at 0.7–6 GHz," *AIP Adv.*, vol. 7, no. 5, 2017, Art. no. 056606.

[59] H. Kurata, K. Shirakawa, O. Nakazima, and K. Murakami, "Study of thin film micro transformer with high operating frequency and coupling coefficient," *IEEE Trans. Magn.*, vol. 29, no. 6, pp. 3204–3206, Nov. 1993.

[60] D. Flynn, A. Toon, L. Allen, R. Dhariwal, and M. P. Desmulliez, "Characterization of core materials for microscale magnetic components operating in the megahertz frequency range," *IEEE Trans. Magn.*, vol. 43, no. 7, pp. 3171–3180, Aug. 2007.

[61] Y. Gao *et al.*, "Power-efficient voltage tunable RF integrated magnetoelectric inductors with FeGaB/Al_2O_3 multilayer films," in *Proc. IEEE MTT-S Int. Microw. Symp.*, 2014, pp. 1–4.

[62] J. Mullenix, A. El-Ghazaly, and S. X. Wang, "Integrated transformers with sputtered laminated magnetic core," *IEEE Trans. Magn.*, vol. 49, no. 7, pp. 4021–4027, Jul. 2013.

[63] A. El-Ghazaly, R. M. White, and S. X. Wang, "Gigahertz-band integrated magnetic inductors," *IEEE Trans. Microw. Theory Techn.*, vol. 65, no. 12, pp. 4893–4900, Dec. 2017.

[64] C. Kittel, "On the theory of ferromagnetic resonance absorption," *Phys. Rev.*, vol. 73, no. 2, 1948, Art. no. 155.

[65] M. Yamaguchi, S. Bae, K. H. Kim, K. Tan, T. Kusumi, and K. Yamakawa, "Ferromagnetic RF integrated inductor with closed magnetic circuit structure," in *IEEE MTT-S Int. Microw. Symp. Dig.*, Jun. 2005, pp. 351–354.

[66] M. Yamaguchi *et al.*, "Magnetic RF integrated thin-film inductors," in *IEEE MTT-S Int. Microw. Symp. Dig.*, Jun. 2000, pp. 205–208.

[67] J. Salvia, J. A. Bain, and C. P. Yue, "Tunable on-chip inductors up to 5 GHz using patterned permalloy laminations," in *Proc. IEEE Int. Electron Devices Meeting*, Dec. 2005, pp. 943–946.

[68] D. S. Gardner, G. Schrom, F. Paillet, B. Jamieson, T. Karnik, and S. Borkar, "Review of on-chip inductor structures with magnetic films," *IEEE Trans. Magn.*, vol. 45, no. 10, pp. 4760–4766, Oct. 2009.

[69] P. Park, C. S. Kim, M. Y. Park, S. D. Kim, and H. K. Yu, "Variable inductance multilayer inductor with MOSFET switch control," *IEEE Electron Device Lett.*, vol. 25, no. 3, pp. 144–146, Mar. 2004.

[70] A. Shirane, H. Ito, N. Ishihara, and K. Masu, "Planar solenoidal inductor in radio frequency micro-electro-mechanical systems technology for variable inductor with wide tunable range and high quality factor," *Jpn. J. Appl. Phys.*, vol. 51, no. 5S, 2012, Art. no. 05EE02.

[71] J. I. Kim and D. Peroulis, "Tunable MEMS spiral inductors with optimized RF performance and integrated large-displacement electrothermal actuators," *IEEE Trans. Microw. Theory Techn.*, vol. 57, no. 9, pp. 2276–2283, Oct. 2009.

[72] I. Zine-El-Abidine, M. Okoniewski, and J. G. McRory, "RF MEMs tunable inductor using bimorph microactuators," in *Proc. IEEE Int. Conf. MEMS, NANO Smart Syst.*, Jul. 2005, pp. 436–437.

[73] A. Bhattacharya, D. Mandal, and T. K. Bhattacharyya, "A 1.3–2.4-GHz 3.1-mW VCO using electro-thermo-mechanically tunable self-assembled MEMS inductor on HR substrate," *IEEE Trans. Microw. Theory Techn.*, vol. 63, no. 2, pp. 459–469, Feb. 2015.

[74] D. M. Fang, Q. Yuan, X. H. Li, and H. X. Zhang, "Electrostatically driven tunable radio frequency inductor," *Microsyst. Technol.*, vol. 16, no. 12, 2010, pp. 2119–2122.

[75] M. Vroubel, Y. Zhuang, B. Rejaei, and J. N. Burghartz, "Integrated tunable magnetic RF inductor," *IEEE Electron Device Lett.*, vol. 25, no. 12, pp. 787–789, Jan. 2005.

[76] T. Wang *et al.*, "Novel electrically tunable microwave solenoid inductor and compact phase shifter utilizing permaloy and PZT thin films," *IEEE Trans. Microw. Theory Techn.*, vol. 65, no. 10, pp. 3569–3577, Oct. 2017.

[77] T. Wang *et al.*, "Integrating nanopatterned ferromagnetic and ferroelectric thin films for electrically tunable RF applications," *IEEE Trans. Microw. Theory Techn.*, vol. 65, no. 2, pp. 504–512, Feb. 2016.

[78] J. Lou, D. Reed, M. Liu, and N. X. Sun, "Electrostatically tunable magnetoelectric inductors with large inductance tunability," *Appl. Phys. Lett.*, vol. 94, no. 11, 2009, Art. no. 112508.

[79] H. Lin *et al.*, "Voltage tunable magnetoelectric inductors with improved operational frequency and quality factor for power electronics," *IEEE Trans. Magn.*, vol. 51, no. 1, pp. 1–5, Jan. 2014.

[80] S. Jiang, Y. Liu, Z. Mei, J. Peng, and C. M. Lai, "A magnetic integrated LCL–EMI filter for a single-phase SiC-MOSFET grid-connected inverter," *IEEE J. Emerg. Sel. Topics Power Electron.*, vol. 8, no. 1, pp. 601–617, Mar. 2020.

[81] J. Fang, H. Li, and Y. Tang, "A magnetic integrated LLCL filter for grid-connected voltage-source converters," *IEEE Trans. Power Electron.*, vol. 32, no. 3, pp. 1725–1730, Sep. 2016.

[82] W. Wu, C. S. Tsai, C. C. Lee, H. J. Yoo, H. Hopster, and D. L. Mills, "Ferromagnetic Fe/Ag-gaas waveguide structures for wideband microwave integrated notch filter devices," in *58th DRC, Device Res. Conf., Dig.*, Jun. 2000, pp. 51–52.

[83] I. Harward, R. E. Camley, and Z. Celinski, "On-wafer magnetically tunable millimeter wave notch filter using *M*-phase Ba hexagonal ferrite/Pt thin films on Si," *Appl. Phys. Lett.*, vol. 105, no. 17, 2014, Art. no.173503.

[84] C. S. Tsai *et al.*, "Tunable wideband microwave band-stop and band-pass filters using YIG/GGG-GaAs layer structures," *IEEE Trans. Magn.*, vol. 41, no. 10, pp. 3568–3570, Nov. 2005.

[85] Y. Y. Song, C. L. Ordóñez-Romero, and M. Wu, "Millimeter wave notch filters based on ferromagnetic resonance in hexagonal barium ferrites," *Appl. Phys. Lett.*, vol. 95, no. 14, 2009, Art. no. 142506.

[86] H. Lin *et al.*, "Tunable RF band-pass filters based on NEMS magnetoelectric resonators," in *Proc. IEEE MTT-S Int. Microw. Symp.*, May 2016, pp. 1–4.

[87] K. Entesari and G. M. Rebeiz, "A differential 4-bit 6.5-10-GHz RF MEMS tunable filter," *IEEE Trans. Microw. Theory Techn.*, vol. 53, no. 3, pp. 1103–1110, Mar. 2005.

[88] C. C. Cheng and G. M. Rebeiz, "High Q 4–6-GHz suspended stripline RF MEMS tunable filter with bandwidth control," *IEEE Trans. Microw. Theory Techn.*, vol. 59, no. 10, pp. 2469–2476, Oct. 2011.

[89] V. Sekar, M. Armendariz, and K. Entesari, "A 1.2–1.6-GHz substrate-integrated-waveguide RF MEMS tunable filter," *IEEE Trans. Microw. Theory Techn.*, vol. 59, no. 4, pp. 866–876, Apr. 2011.

[90] S. M. Hanna and S. Zeroug, "Single and coupled MSW resonators for microwave channelizers," *IEEE Trans. Magn.*, vol. TSM-24, no. 6, pp. 2808–2810, Jun. 1988.

[91] W. S. Ishak and K. W. Chang, "Tunable microwave resonators using magnetostatic wave in YIG films," *IEEE Trans. Microw. Theory Techn.*, vol. MTT-34, no. 12, pp. 1383–1393, Dec. 1986.

[92] J. Wu, X. Yang, S. Beguhn, J. Lou, and N. X. Sun, "Nonreciprocal tunable low-loss bandpass filters with ultra-wideband isolation based on magnetostatic surface wave," *IEEE Trans. Microw. Theory Techn.*, vol. 60, no. 12, pp. 3959–3968, Dec. 2012.

[93] D. B. Miron, *Small Antenna Design*. Amsterdam, The Netherlands; New York, NY, USA: Elsevier, 2006.

[94] J. Volakis, C. C. Chen, and K. Fujimoto, *Small Antennas: Miniaturization Techniques & Applications*. New York, NY, USA: McGraw Hill, 2009.

[95] O. Staub, J. F. Zurcher, A. K. Skrivervik, and J. R. Mosig, "PCS antenna design: The challenge of miniaturisation," in *Proc. IEEE Antennas Propag. Soc. Int. Symp./USNC/URSI Nat. Radio Sci. Meeting*, Jul. 1999, pp. 548–551.

[96] C. Pfeiffer, "Fundamental efficiency limits for small metallic antennas," *IEEE Trans. Antennas Propag.*, vol. 65, no. 4, pp. 1642–1650, Apr. 2017.

[97] L. J. Chu, “Physical limitations of omni-directional antennas,” *J. Appl. Phys.*, vol. 19, no. 12, pp. 1163–1175, 1948.

[98] R. F. Harrington, “Effect of antenna size on gain, bandwidth, and efficiency,” *J. Res. Nat. Bur. Standards D, Radio Propag.*, vol. 64, no. 1, pp. 1–12, 1960.

[99] R. C. Hansen, “Fundamental limitations in antennas,” *Proc. IEEE*, vol. 69, no. 2, pp. 170–182, 1981.

[100] Z. Yao, Y. E. Wang, S. Keller, and G. P. Carman, “Bulk acoustic wave-mediated multiferroic antennas: Architecture and performance bound,” *IEEE Trans. Antennas Propag.*, vol. 63, no. 8, pp. 3335–3344, Aug. 2015.

[101] J. P. Domann and G. P. Carman, “Strain powered antennas,” *J. Appl. Phys.*, vol. 121, no. 4, 2017, Art. no. 044905.

[102] C. Dong *et al.*, “A portable very low frequency (VLF) communication system based on acoustically actuated magnetoelectric antennas,” *IEEE Antennas Wireless Propag. Lett.*, vol. 19, no. 3, pp. 398–402, Jan. 2020.

[103] T. Karacolak, A. Z. Hood, and E. Topsakal, “Design of a dual-band implantable antenna and development of skin mimicking gels for continuous glucose monitoring,” *IEEE Trans. Microw. Theory Techn.*, vol. 56, no. 4, pp. 1001–1008, May 2008.

[104] T. Rupp, B. D. Truong, S. Williams, and S. Roundy, “Magnetoelectric transducer designs for use as wireless power receivers in wearable and implantable applications,” *Materials*, vol. 12, no. 3, 2019, Art. no. 512.

[105] F. J. Huang, C. M. Lee, C. L. Chang, L. K. Chen, T. C. Yo, and C. H. Luo, “Rectenna application of miniaturized implantable antenna design for triple-band biotelemetry communication,” *IEEE Trans. Antennas Propag.*, vol. 59, no. 7, pp. 2646–2653, Jul. 2011.

[106] C. M. Lee, T. C. Yo, and C. H. Luo, “Compact broadband stacked implantable antenna for biotelemetry with medical devices,” in *Proc. IEEE Annu. Wireless Microw. Technol. Conf.*, Dec. 2006, pp. 1–4.

[107] M. Zaeimbashi *et al.*, “NanoNeuroRFID: A wireless implantable device based on magnetoelectric antennas,” *IEEE J. Electromagn., RF Microw. Med. Biol.*, vol. 3, no. 3, pp. 206–215, Mar. 2019.

[108] H. Lin *et al.*, “NEMS magnetoelectric antennas for biomedical application,” in *Proc. IEEE Int. Microw. Biomed. Conf.*, Jun. 2018, pp. 13–15.

[109] D. Robbes, “Highly sensitive magnetometers—A review,” *Sens. Actuators A, Phys.*, vol. 129, no. 1/2, pp. 86–93, 2006.

[110] M. Schmelz, *et al.*, “Sub-fT/Hz1/2 resolution and field-stable SQUID magnetometer based on low parasitic capacitance sub-micrometer cross-type Josephson tunnel junctions,” *Physica C, Supercond. Appl.*, vol. 482, pp. 27–32, 2012.

[111] B. Gojdka *et al.*, “Fully integrable magnetic field sensor based on delta-E effect,” *Appl. Phys. Lett.*, vol. 99, no. 22, 2011, Art. no. 223502.

[112] Y. Hui, T. Nan, N. X. Sun, and M. Rinaldi, “High resolution magnetometer based on a high frequency magnetoelectric MEMS-CMOS oscillator,” *J. Microelectromech. Syst.*, vol. 24, no. 1, pp. 134–143, 2014.

[113] M. Li *et al.*, “Ultra-sensitive NEMS magnetoelectric sensor for picotesla DC magnetic field detection,” *Appl. Phys. Lett.*, vol. 110, no. 14, 2017, Art. no. 143510.

[114] C. Muşuroi, M. Oproiu, M. Volmer, and I. Firastrau, “High sensitivity differential giant magnetoresistance (GMR) based sensor for non-contacting DC/AC current measurement,” *Sensors*, vol. 20, no. 1, 2020, Art. no. 323.

[115] Z. Jin, M. N. Sam, M. Oogane, and Y. Ando, “Serial MTJ-based TMR sensors in bridge configuration for detection of fractured steel bar in magnetic flux leakage testing,” *Sensors*, vol. 21, no. 2, 2021, Art. no. 668.

[116] E. S. Leland, P. K. Wright, and R. M. White, “A MEMS AC current sensor for residential and commercial electricity end-use monitoring,” *J. Micromech. Microeng.*, vol. 19, no. 9, 2009, Art. no. 094018.

[117] S. B. Lao, S. S. Chauhan, T. E. Pollock, T. Schröder, I. S. Cho, and A. Salehian, “Design, fabrication and temperature sensitivity testing of a miniature piezoelectric-based sensor for current measurements,” *Actuators*, vol. 3, no. 3, pp. 162–181, 2014.

[118] F. Niekiel *et al.*, “Highly sensitive MEMS magnetic field sensors with integrated powder-based permanent magnets,” *Sens. Actuators A, Phys.*, vol. 297, 2019, Art. no. 111560.

[119] L. Long and S. Zhong, “A MEMS torsion magnetic sensor with reflective blazed grating integration,” *J. Micromech. Microeng.*, vol. 26, no. 7, 2016, Art. no. 075004.

[120] L. Long, M. Wang, and S. Zhong, “A torsion MEMS magnetic sensor with permanent magnet and fiber-optic detection,” *IEEE Sens. J.*, vol. 16, no. 23, pp. 8426–8433, Dec. 2016.

[121] S. O. Choi, S. Kawahito, Y. Matsumoto, M. Ishida, and Y. Tadokoro, “An integrated micro fluxgate magnetic sensor,” *Sens. Actuators A, Phys.*, vol. 55, no. 2/3, pp. 121–126, 1996.

[122] Y. Wang, J. Li, and D. Viehland, “Magnetoelectrics for magnetic sensor applications: Status, challenges and perspectives,” *Mater. Today*, vol. 17, no. 6, pp. 269–275, 2014.

[123] J. Gao, J. Das, Z. Xing, J. Li, and D. Viehland, “Comparison of noise floor and sensitivity for different magnetoelectric laminates,” *J. Appl. Phys.*, vol. 108, no. 8, 2010, Art. no. 084509.

[124] L. Shen *et al.*, “Magnetoelectric nonlinearity in magnetoelectric laminate sensors,” *J. Appl. Phys.*, vol. 110, no. 11, 2011, Art. no. 114510.

[125] J. Das, J. Gao, Z. Xing, J. F. Li, and D. Viehland, “Enhancement in the field sensitivity of magnetoelectric laminate heterostructures,” *Appl. Phys. Lett.*, vol. 95, no. 9, 2009, Art. no. 092501.

[126] M. Li, D. Berry, J. Das, D. Gray, J. Li, and D. Viehland, “Enhanced sensitivity and reduced noise floor in magnetoelectric laminate sensors by an improved lamination process,” *J. Amer. Ceram. Soc.*, vol. 94, no. 11, pp. 3738–3741, 2011.

[127] J. Zhai, Z. Xing, S. Dong, J. Li, and D. Viehland, “Detection of pico-Tesla magnetic fields using magneto-electric sensors at room temperature,” *Appl. Phys. Lett.*, vol. 88, no. 6, 2006, Art. no. 062510.

[128] J. Gao, Y. Wang, M. Li, Y. Shen, J. Li, and D. Viehland, “Quasi-static ($f< 10-2$ Hz) frequency response of magnetoelectric composites based magnetic sensor,” *Mater. Lett.*, vol. 85, pp. 84–87, 2012.

[129] P. Zhao *et al.*, “Fabrication and characterization of all-thin-film magnetoelectric sensors,” *Appl. Phys. Lett.*, vol. 94, no. 24, 2009, Art. no. 243507.

[130] E. Yarar *et al.*, “Inverse bilayer magnetoelectric thin film sensor,” *Appl. Phys. Lett.*, vol. 109, no. 2, 2016, Art. no. 022901.

[131] T. Nan, Y. Hui, M. Rinaldi, and N. X. Sun, “Self-biased 215MHz magnetoelectric NEMS resonator for ultra-sensitive DC magnetic field detection,” *Sci. Rep.*, vol. 3, no. 1, pp. 1–6, 2013.

[132] R. Jahns, H. Greve, E. Woltermann, E. Quandt, and R. H. Knochel, “Noise performance of magnetometers with resonant thin-film magnetoelectric sensors,” *IEEE Trans. Instrum. Meas.*, vol. 60, no. 8, pp. 2995–3001, Sep. 2011.

[133] A. A. Chlaihawi *et al.*, “Novel screen printed flexible magnetoelectric thin film sensor,” *Procedia Eng.*, vol. 168, pp. 684–687, 2016.

[134] R. Jahns, H. Greve, E. Woltermann, E. Quandt, and R. Knöchel, “Sensitivity enhancement of magnetoelectric sensors through frequency-conversion,” *Sens. Actuators A, Phys.*, vol. 183, pp. 16–21, 2012.

[135] V. Röbisch *et al.*, “Exchange biased magnetoelectric composites for magnetic field sensor application by frequency conversion,” *J. Appl. Phys.*, vol. 117, no. 17, 2015, Art. no. 17B513.

[136] S. Salzer *et al.*, “Generalized magnetic frequency conversion for thin-film laminate magnetoelectric sensors,” *IEEE Sens. J.*, vol. 17, no. 5, pp. 1373–1383, May 2016.

[137] D. P. Arnold and N. Wang, “Permanent magnets for MEMS,” *J. Microelectromech. Syst.*, vol. 18, no. 6, pp. 1255–1266, 2009.

[138] O. Berkh, Y. Rosenberg, Y. Shacham-Diamand, and E. Gileadi, “Deposition of CoPtP films from citric electrolyte,” *Microelectron. Eng.*, vol. 84, no. 11, pp. 2444–2449, 2007.

[139] A. Walther, D. Givord, N. M. Dempsey, K. Khlopkov, and O. Gutfleisch, “Structural, magnetic, and mechanical properties of 5 μm thick smco films suitable for use in microelectromechanical systems,” *J. Appl. Phys.*, vol. 103, no. 4, 2008, Art. no. 043911.

[140] F. J. Cadieu, L. Chen, and B. Li, “Enhanced magnetic properties of nanophase SmCo5 film dispersions,” *IEEE Trans. Magn.*, vol. 37, no. 4, pp. 2570–2572, Apr. 2001.

[141] S. Schwarzer, B. Pawlowski, A. Rahmig, and J. Töpfer, “Permanent magnetic thick films from remanence optimized NdFeB-inks,” *J. Mater. Sci., Mater. Electron.*, vol. 15, no. 3, pp. 165–168, 2004.

[142] Y. He *et al.*, “High-performance on-chip hot-pressed NdFeB hard magnets for MEMS applications,” *IEEE Trans. Magn.*, vol. 57, no. 4, pp. 1–4, Feb. 2021.

[143] B. G. Compton *et al.*, “Direct-write 3D printing of NdFeB bonded magnets,” *Mater. Manuf. Processes*, vol. 33, no. 1, pp. 109–113, 2018.

[144] L. Jiang, A. Gokce, F. C. S. Silva, and E. R. Nowak, “Zigzag-shaped AMR magnetic sensors: Transfer characteristics and noise,” in *Noise and Information in Nanoelectronics, Sensors, and Standards III*, Bellingham WA, USA: SPIE, May 2005, vol. 5846, pp. 156–168.

[145] H. Eberta, A. Vernesa, and J. Banhartb, “Magnetoresistance, anisotropic,” *Encyclopedia of Materials: Science and Technology.*, 2nd ed. Oxford, U.K.: Pergamon Press, 2001, pp. 5079–5083.

[146] L. Jogschies *et al.*, “Recent developments of magnetoresistive sensors for industrial applications,” *Sensors*, vol. 15, no. 11, pp. 28665–28689, 2015.

[147] W. F. Egelhoff, *et al.*, “Critical challenges for picoTesla magnetic-tunnel-junction sensors,” *Sens. Actuators A, Phys.*, vol. 155, no. 2, pp. 217–225, 2009.

[148] S. Yuasa, T. Nagahama, A. Fukushima, Y. Suzuki, and K. Ando, “Giant room-temperature magnetoresistance in single-crystal Fe/MgO/Fe magnetic tunnel junctions,” *Nature Mater.*, vol. 3, no. 12, pp. 868–871, 2004.

[149] S. S. Parkin *et al.*, “Giant tunnelling magnetoresistance at room temperature with MgO (100) tunnel barriers,” *Nature Mater.*, vol. 3, no. 12, pp. 862–867, 2004.

[150] S. Ikeda *et al.*, “Tunnel magnetoresistance of 604% at 300 K by suppression of Ta diffusion in CoFeB/MgO/CoFeB pseudo-spin-valves annealed at high temperature,” *Appl. Phys. Lett.*, vol. 93, no. 8, 2008, Art. no. 082508.

[151] N. F. Mott, “The resistance and thermoelectric properties of the transition metals,” *Proc. Roy. Soc. Lond. A, Math. Phys. Sci.*, vol. 156, no. 888, pp. 368–382, 1936.

[152] M. N. Baibich *et al.*, “Giant magnetoresistance of (001) Fe/(001) Cr magnetic superlattices,” *Phys. Rev. Lett.*, vol. 61, no. 21, 1988, Art. no. 2472.

[153] B. Dieny *et al.*, “Magnetotransport properties of magnetically soft spin-valve structures,” *J. Appl. Phys.*, vol. 69, no. 8, pp. 4774–4779, 1991.

[154] S. S. P. Parkin, N. More, and K. P. Roche, “Oscillations in exchange coupling and magnetoresistance in metallic superlattice structures: Co/Ru, Co/Cr, and Fe/Cr,” *Phys. Rev. Lett.*, vol. 64, no. 19, 1990, Art. no. 2304.

[155] S. S. P. Parkin, “Origin of enhanced magnetoresistance of magnetic multilayers: Spin-dependent scattering from magnetic interface states,” *Phys. Rev. Lett.*, vol. 71, no. 10, 1993, Art. no. 1641.

[156] J. S. Moodera, L. R. Kinder, T. M. Wong, and R. Meservey, “Large magnetoresistance at room temperature in ferromagnetic thin film tunnel junctions,” *Phys. Rev. Lett.*, vol. 74, no. 16, 1995, Art. no. 3273.

[157] C. Muşuroi, M. Oproiu, M. Volmer, J. Neamtu, M. Avram, and E. Helerea, “Low field optimization of a non-contacting high-sensitivity GMR-based DC/AC current sensor,” *Sensors*, vol. 21, no. 7, 2021, Art. no. 2564.

[158] A. Barman, S. Mondal, S. Sahoo, and A. De, “Magnetization dynamics of nanoscale magnetic materials: A perspective,” *J. Appl. Phys.*, vol. 128, no. 17, 2020, Art. no. 170901.

[159] M. Akiyama, T. Kamohara, K. Kano, A. Teshigahara, Y. Takeuchi, and N. Kawahara, “Enhancement of piezoelectric response in scandium aluminum nitride alloy thin films prepared by dual reactive cosputtering,” *Adv. Mater.*, vol. 21, no. 5, pp. 593–596, 2009.

[160] S. Fichtner, N. Wolff, F. Lofink, L. Kienle, and B. Wagner, “AlScN: A III-V semiconductor based ferroelectric,” *J. Appl. Phys.*, vol. 125, no. 11, 2019, Art. no. 114103.

[161] F. Parsapour, V. Pashchenko, P. Nicolay, and P. Murali, “Material constants extraction for AlScN thin films using a dual mode baw resonator,” in *Proc. IEEE Micro Electro Mech. Syst.*, 2018, pp. 763–766.

[162] F. Parsapour *et al.*, “Ex-situ AlN seed layer for (0001)-textured al 0.84 sc 0.16 n thin films grown on SiO$_2$ substrates,” in *Proc. IEEE Int. Ultrason. Symp.*, 2017, pp. 1–4.

[163] R. H. Olsson, Z. Tang, and M. D’Agati, “Doping of aluminum nitride and the impact on thin film piezoelectric and ferroelectric device performance,” in *Proc. IEEE Custom Integr. Circuits Conf.*, Mar. 2020, pp. 1–6.

[164] P. M. Mayrhofer, P. Å. Persson, A. Bittner, and U. Schmid, “Properties of Sc x Al 1-x N (x= 0.27) thin films on sapphire and silicon substrates upon high temperature loading,” *Microsyst. Technol.*, vol. 22, no. 7, pp. 1679–1689, 2016.

[165] S. Chauhan *et al.*, “Multiferroic, magnetoelectric and optical properties of Mn doped BiFeO3 nanoparticles,” *Solid State Commun.*, vol. 152, no. 6, pp. 525–529, 2012.

[166] A. Hussain *et al.*, “The development of BiFeO$_3$-based ceramics,” *Chin. Sci. Bull.*, vol. 59, no. 36, pp. 5161–5169, 2014.

[167] X. Chen *et al.*, “Structure, ferroelectric and piezoelectric properties of multiferroic Bi0. 875Sm0. 125FeO3 ceramics,” *J. Alloys Compounds*, vol. 541, pp. 173–176, 2012.

[168] R. K. Mishra, D. K. Pradhan, R. N. P. Choudhary, and A. Banerjee, “Effect of yttrium on improvement of dielectric properties and magnetic switching behavior in BiFeO3,” *J. Phys., Condens. Matter*, vol. 20, no. 4, 2008, Art. no. 045218.

[169] X. Liang *et al.*, “Soft magnetism, magnetostriction, and microwave properties of Fe-Ga-C alloy films,” *IEEE Magn. Lett.*, vol. 10, pp. 1–5, Dec. 2018.

[170] X. C. Kan *et al.*, “Magnetic/structural phase diagram and zero temperature coefficient of resistivity in GaCFe3− xCox (0≤ x≤ 3.0),” *J. Alloys Compounds*, vol. 663, pp. 94–99, 2016.

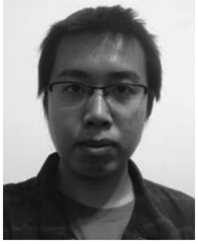

YIFAN HE received the B.E. degree in electrical engineering from Tianjin University, Tianjin, China, in 2014, and the M.S. degree in electrical and computer engineering from Northeastern University, Boston, MA, USA, in 2016, where he is currently working toward the Ph.D. degree in electrical engineering. His research interests include magnetic material and its application in RF/microwave devices, energy harvesting devices.

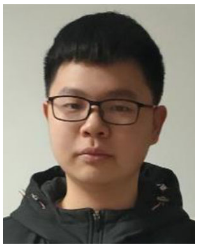

BIN LUO received the B.E. degree in electrical engineering from the Huazhong University of Science and Technology, Wuhan, China, in 2020. He is currently working toward the Ph.D. degree in electrical engineering with Northeastern University, Boston, MA, USA. His research interests include gas discharge plasma and lightning physics, electrical breakdown and lightning protection, computational chemical kinetics, fluid dynamics and electromagnetics, novel magnetic, ferroelectric, and multiferroic materials and their applications in RF/microwave electronics and spintronics, sensors and quantum devices.

NIAN-XIANG SUN (Fellow, IEEE) received the Ph.D. degree from Stanford University, Stanford, CA, USA. He was a Scientist with IBM, Armonk, NY, USA, and Hitachi Global Storage Technologies, San Jose, CA, USA. He is currently a Professor with the Electrical and Computer Engineering Department and the Director of the W.M. Keck Laboratory for Integrated Ferroics, Northeastern University, Boston, MA, USA, and the Founder and a Chief Technical Advisor of Winchester Technologies, LLC, Burlington, MA, USA. He has authored or coauthored more than 280 publications. He holds more than 20 patents and patent applications. His research interests include novel magnetic, ferroelectric, and multiferroic materials, devices, and subsystems. One of his articles was selected as the Ten Most Outstanding Full Papers in the Past Decade (2001–2010) in *Advanced Functional Materials*. Dr. Sun was the recipient of the NSF CAREER Award, the ONR Young Investigator Award, and the Søren Buus Outstanding Research Award. He is an editor of the *Sensors* and IEEE TRANSACTIONS ON MAGNETICS and a Fellow of the Institute of Physics and the Institution of Engineering and Technology. He has given more than 180 plenary/keynote/invited presentations and seminars.